Title
Comparison of Acoustically Coupled Combustion Studies Under Laminar and Turbulent Conditions

Author
kiani, sarina

Publication Date
2021

Peer reviewed|Thesis/dissertation

UNIVERSITY OF CALIFORNIA
Los Angeles

Comparison of Acoustically Coupled Combustion Studies Under Laminar and Turbulent Conditions

A thesis submitted in partial satisfaction
of the requirements for the degree
Master of Science in Aerospace Engineering

by

Sarina Kiani

2021

ABSTRACT OF THE THESIS

Comparison of Acoustically Coupled Combustion Studies Under Laminar and Turbulent Conditions

by

Sarina Kiani
Master of Science in Aerospace Engineering
University of California, Los Angeles, 2021
Professor Ann R. Karagozian, Chair

In this study, the acoustically coupled combustion instability experiments conducted at the Air Force Research Laboratory (AFRL/RQR) located at Edwards Air Force Base, and our research group at the Energy and Propulsion Research Laboratory (EPRL) at UCLA are compared. The main goal is to investigate a comparison of gaseous methane flames under oscillatory acoustic fields subjected to laminar (Re ranging from 20 to 100) and turbulent (Re of 5300) conditions using two alternative burner configurations of single and coaxial jets. This study also explores the different flow regimes and the parameters causing high-frequency transverse mode instabilities in fuel jet combustion relevant to liquid rocket engines. At the Air Force Research Laboratory, the experiments are focused on turbulent jet combustion under acoustic forcing at pressure nodes and anti-nodes with the following burner configurations: a single methane jet surrounded by a low-velocity oxidizer co-flow and a coaxial jet with annular oxidizer flow and the low-velocity co-flow. In a collaborative effort, our research group at the EPRL at UCLA explores the gaseous laminar reactive methane microjets under acoustic forcing at a configuration closer to the pressure node for two burner configurations

of single and coaxial jets. The main difference between the configuration setups at UCLA and AFRL is the absence of low-velocity co-flow at the UCLA EPRL experiments. To study such combustion instabilities, the data are acquired by high-speed schlieren, OH^* chemiluminescence, and high-speed imaging. Then, the collected data are analyzed using proper orthogonal decomposition (POD) and dynamic mode decomposition (DMD) to quantify the flames dynamics.

Similar dynamical patterns are observed by comparing the single and coaxial jets subjected to laminar and turbulent conditions. For instance, a single jet with Reynolds number 65 has similar phase portraits as the single turbulent jet with Reynolds number 5300. Both exhibit the locking-in of the oscillating flame under the applied acoustic forcing and a periodic behavior. Additionally, no natural instability is observed for the laminar and turbulent single jets. The second burner configuration, the coaxial jet, also demonstrates similarities between the POD modes. A similar annular to inner velocity ratio of $R = 0.3$ is selected for the coaxial jets. UCLA and AFRL reveal similar dynamical characteristics for the acoustically coupled laminar and turbulent fuel jet studies. This kind of understanding could be beneficial in developing reduced order models (ROMs) for such combustion instabilities, which eventually could be used in controlling and predicting such instabilities based on operating conditions or configuration changes. Additionally, these similarities reveal the value of low Reynolds number reactive microjet dynamics in understanding high Reynolds numbers experiments, but at a smaller scale with a lower cost.

The thesis of Sarina Kiani is approved.

Kunihiko Taira

Raymond M. Spearrin

Ann R. Karagozian, Committee Chair

University of California, Los Angeles

2021

TABLE OF CONTENTS

LIST OF FIGURES

LIST OF TABLES

Nomenclature

λ	Wavelength associated to resonant frequencies
c	Speed of sound
f_a	Acoustic frequency
G	Rayleigh index
L_x	Acoustic waveguide's transverse length
L_y	Acoustic waveguide's height
L_z	Acoustic waveguide's width
n_i	Integers
P'	Local pressure perturbation
P'_{max}	Pressure oscillation amplitude at pressure anti-node
PAN	Pressure anti-node
PN	Pressure node
q'	Unsteady heat release
R	Velocity ratio (annular oxidizer-to-inner methane jet)
Re	Reynolds number
T	Acoustic period
u'	Local velocity oscillation amplitude
u'_{max}	Velocity oscillation amplitude at pressure anti-node
x	Location x

ACKNOWLEDGMENTS

First and foremost, I would like to express my most profound appreciation to my research advisor, Professor Ann Karagozian, for her unwavering support and guidance throughout my Master's degree. Her encouragement, patience, and insightful feedbacks helped me write this thesis and complete my degree. I'd also like to extend my gratitude to Andres Vargas, my colleague, for his helpful contributions to writing this thesis and conducting research throughout my graduate studies. Many thanks to my parents for their continuous guidance and support.

This research was funded by the Air Force Office of Scientific Research (AFOSR) under Award No. FA9550-19-1-0096, with Dr. Mitat Birkan as program manager, and by a UCLA MAE graduate fellowship.

CHAPTER 1

Introduction and Background

1.1 Combustion Instabilities

Combustion instabilities pose a significant challenge in developing high-performing jet propulsion systems and gas turbine combustors [Candel, 1992, McManus et al., 1993]. By definition, instabilities are the unwanted effects of flow parameters' large oscillations [Candel, 1992]. Low-frequency and amplified pressure oscillations are catastrophic by imposing undesirable mechanical vibrations through the combustion systems [Candel, 1992]. Analytical modeling of these instabilities is challenging due to the complex nature of the problem, such as nonlinear behavior and coupled interactions. Thus most of the studies on such instabilities are experimental case-by-case work. Although extensive experimental data is necessary for accurate results, the simplified analytical equations could predict the model with uncertainty [McManus et al., 1993].

The instabilities' nonlinear behavior is due to the exothermic chemical reaction and the coupling of chamber acoustics to such reactions associated with the flame. These large oscillations in pressure in turn create perturbations in the velocity, which then enhance oscillations in heat release and hence in turn in the pressure, creating a feedback cycle as shown in Figure 1.1 [Rayleigh, 1878]. As the feedback cycle ensues, significant growth in the instabilities and coupling between the reaction and flow/pressure oscillations takes place, not only reducing the system's performance and causing early erosion of chamber walls [Candel, 1992], but also potentially leading to catastrophic destruction of the combustion chamber, as

was prevalent during the development of the F1 engine for the Apollo program [Karagozian, 2016]. An additional concern in combustion systems is sustaining the reactive processes and preventing partial/complete blow-off of the flame in connection with large oscillations [Candel, 1992, McManus et al., 1993].

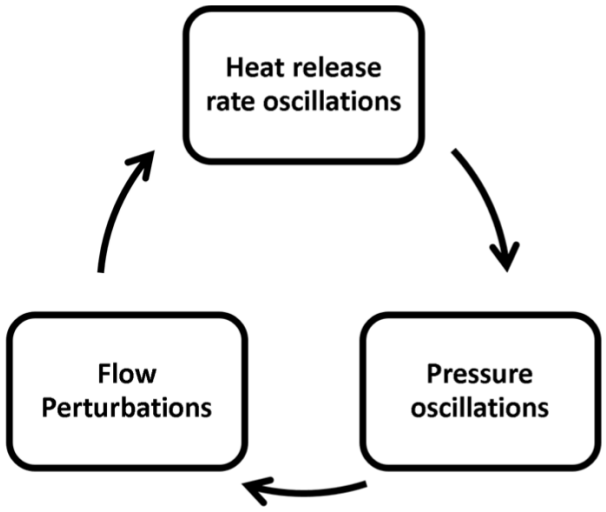

Figure 1.1: Thermo-acoustic instability feedback cycle [Vargas, 2019].

The classical Rayleigh criterion has traditionally been used to quantify the combustion instabilities as they evolve dynamically [Rayleigh, 1878], wherein the oscillations may be sustained if the heat release is in phase with the local pressure fluctuations, or nearly so, and decay when they are out of phase or nearly so [Candel, 1992]. In other words, knowledge of either global or local unsteady heat release and local pressure perturbations can enable understanding and prediction of locally amplified fluctuations. A parameter called the Rayleigh index can be defined to represent the coupling between the unsteady heat release and the pressure perturbations in order to quantify the potential for combustion instability amplification or decay. The Rayleigh index can be mathematically modeled over an acoustic period T at a specific location x, via the following mathematical equation (Equation 1.1). Here q' is the unsteady heat release, P' is the local pressure perturbation, and G is the Rayleigh index [Wu et al., 2019] defined as

$$G(x) = \frac{1}{T} \int_T p'(x,t) q'(x,t) dt. \tag{1.1}$$

The Rayleigh index predicts the thermoacoustic instabilities through the sign of the G value. If the Rayleigh index G is positive, the nonlinear instability is growing. A negative Rayleigh index, on the other hand, implies stable combustion or damping of the instability, at least in a global sense. For some experiments, however, the localized Rayleigh index may be negative when there is a transition in the flame dynamics during acoustic coupling. Our group has seen this in acoustically-coupled liquid droplet experiments, where periodic partial extinction and reignition (PPER) at high amplitude acoustic coupling creates a negative Rayleigh index [Bennewitz et al., 2018, Sim et al., 2019]. PPER is defined as the periodic extinction and reignition of the deflected flame, which is associated with the fluctuations in the oscillatory strain field [Sim et al., 2020]. Negative Rayleigh indices are also observed for single gaseous fuel jets in the presence of acoustic perturbations, corresponding to periodic lift off and reattachment (PLOR) [Sim et al., 2020]. The latter experiment will be described in more detail in this thesis.

The present study aims to control and predict such combustion instabilities based on operating conditions or configuration changes. To do so, a detailed quantification of acoustically coupled flame dynamics is necessary [Wu et al., 2019]. Combustion instabilities became prominent as a major engineering challenge during the development of liquid rocket engines in the 1930s [Culick and Yang, 1995]. For the past seventy years, combustion instability has been under continuous study and development, for both rocket and airbreathing propulsion systems. While actual research of liquid rocket combustion instability started before the 1940s, no significant advancement was done until the end of World War II. The development of large intercontinental ballistic missiles marks a milestone in studying instabilities in liquid rocket engines [Culick and Yang, 1995]. The first step in studying the combustion instabilities is understanding the difference between linear and non-linear instabilities. In the 1960s, the self-triggered instability was considered linear, and dynamic instability resulted

from significant disturbances imposed on a linear system. Based on the research done during 1959-1962, it suggested the use of baffles to prevent dynamic instability [Culick and Yang, 1995].

As noted above, development of the F1 engine for the Apollo program in the 1960s led to further progress in the study of instabilities. The F1 engine underwent 2000 intensive large-scale testing to resolve the issue of combustion instability [Culick and Yang, 1995, Oefelein and Yang, 1993, Candel, 2002]. Unfortunately, these costly experiments were unsuccessful and destroyed a number of combustion chambers. After the unsuccessful testings, research emphasis was placed on improving the F1 engine's injector design to have more stability in the system [Oefelein and Yang, 1993]. In the 1980s, studies focused on investigating combustion instabilities through fuel injection design and active system control. In an active control, an acoustic driver decouples the mechanisms causing fluctuations [Candel, 2002]. Passive control is another control method; however, it is not widely used or preferred due to iterative design requirements and the expensive cost of the experimental trials.

More recently, researchers aim to develop approaches to predict and model these combustion instabilities as well as controlling them. The process includes extensive data acquisition in the laboratories and data analysis to trace similar behaviors. The goal of studies conducted at UCLA EPRL and AFRL is to enable characterization of combustion instabilities using contemporary dynamical analysis tools, enabling future development of reduced order models that can become part of control systems.

1.2 Prior Studies on Acoustically Perturbed Jet Combustion

The above description provides some background on combustion instabilities; the focus will be shifted to acoustically perturbed fuel jet combustion in the following section, which is the main focus of this study. Early laminar jet combustion studies focused on a simplified model of infinitely fast chemistry to quantify fuel jet flame structure (Burke-Schumann model,

described in [Weiss et al., 2018]). In addition to the infinitely fast combustion to predict the flame height, Burke and Schumman assumed a uniform diffusivity with constant axial flow velocities, negligible axial diffusion, and radial convection [Weiss et al., 2018]. The Burke-Schumman model has been confirmed to predict the flame height accordingly if a single diffusion coefficient is used for all the species. Roper [Chung and Law, 1984] modified Burke-Schumann's theory of diffusion flame size using circular burners, including the axial diffusion, radial convection, and axial velocity gradient neglected in the prior study. As a result, Roper concluded that flame length is directly proportional to the flowrate of the fuel. Experimental studies performed by other researchers have confirmed his conclusion [Saito et al., 1986, Li et al., 1995]. However, there have been some arguments [Choudhuri et al., 2002] regarding the range of the burner's diameter for which Roper's theory is applicable.

Numerous studies have examined the coupling between premixed flames and acoustic processes [Preetham et al., 2008, Lieuwen et al., 2000], though only recently have studies at AFRL and UCLA explored non-premixed flames exposed to acoustic perturbations. One recent computational study from Nanyang Technological University explored the response of propane (C3H8) jet diffusion flame to the acoustic waves from loudspeakers [Chen et al., 2017]. Based on Chen's simulation, unsteady heat release is found to depend on the acoustic disturbance frequency and the forcing amplitude. Other studies also reported changes in the flame shape due to acoustic forcing [Chen et al., 2017]. However, the flame shape disturbances were more observable at acoustic velocity anti-nodes or pressure nodes.

The majority of prior studies have been focused on longitudinal acoustic perturbation of the flame structure. Transverse acoustic perturbation, which is our research group's focus, along with that of AFRL, has seen a more limited number of contributions in the literature, and in particular, coaxial reactive jets are not widely studied. This thesis aims to compare combustion instability characteristics between those studied at UCLA, for very low Reynolds numbers, and those studied at AFRL, at high (turbulent) Reynolds numbers, for both single and coaxial jet configurations.

1.3 Present Studies on Acoustically Perturbed Jet Combustion

The topic of dynamic coupling between transverse acoustics and unsteady heat release oscillations is very important. The resonant interactions between coupling modes and flame combustion are directly correlated to the combustion instabilities, which leads to flame blow-off and a decrease in the performance of the mechanisms [Ducruix et al., 2003]. In our research group at the Energy and Propulsion Research Laboratory at UCLA and the Air Force Research Laboratory (AFRL), such flame-acoustic coupling experiments are performed to study the parameters causing the high-frequency transverse mode instabilities. In addition, alternative burner configurations, including single and concentric co-flow burners and various fuel to oxidizer velocity ratios, are investigated to understand such mechanisms responsible for the transverse mode instabilities.

The focus of this study is comparing gaseous flames under oscillatory pressure fields with laminar and turbulent conditions. The work done at the Air Force Research Laboratory (AFRL) focuses on turbulent jets under traverse forcing at pressure nodes and anti-nodes. At the same time, our research group at the Energy and Propulsion Research Laboratory at UCLA studies the gaseous laminar jet diffusion flames under acoustic forcing at a configuration closer to the pressure node. Although both research labs study a similar concept, our scales and flow conditions are vastly different. AFRL investigates a high Reynolds number of 5,300, while at UCLA, we examine Reynolds numbers ranging from 20 to 100. Although the acoustic forcing is performed on two different laminar and turbulent flow regimes, similar behaviors are identified. The comparison of the behaviors is discussed in detail in chapter three of this document. To better understand the difference in the scaling of two experimental setups, the parameters are non-dimensionalized, and behavioral trends are classified. Proper Orthogonal Decomposition (POD) is an analysis tool used to extract the relevant characteristics such as mode shapes to help understand the instabilities.

The comparison between the laminar and turbulent flames under acoustic forcing focuses

on the flame dynamics rather than the chemical kinetics since only one type of fuel (gaseous methane) is used in the experiments. However, it is essential to note that different fuels would have different chemical kinetic timescales and thus affect not only the heat release rate but also the combustion-acoustic coupling dynamics [Bennewitz et al., 2018]. Our research group at UCLA has explored the dependence of the droplet periodic partial extinction and reignition (PPER) phenomena on fuel type and hence on kinetic effects [Bennewitz et al., 2018], and this kind of exploration for alternative gaseous fuels could also take place in the future.

1.3.1 Air Force Research Laboratory (AFRL)

At the Air Force Research Laboratory (AFRL), acoustically coupled reactive gaseous jet experiments have been conducted by Miguel Plascencia as part of his Ph.D. dissertation [Plascencia Quiroz, 2021]. This research aims to understand the coupling of the flame and acoustics to control the decay/growth of the combustion instabilities. By the use of OH^* chemiluminescence as well as Schlieren imaging, the dynamics of the acoustic-flame coupling are explored. Two different jet configurations are used to study the dynamic coupling between flame and acoustics during combustion instability. A detailed overview of these configurations is included in chapter two of this document.

The first configuration is a single methane jet with co-flow. The co-flow oxygen concentration (60 percent N_2 + 40 percent O_2) is selected to keep the flame anchored at a velocity of 1 m/s. Subsequently, the study of acoustically coupled combustion was performed on a single burner with a turbulent Reynolds number (5,300) for fuel jets placed at a pressure node and pressure anti-node locations affiliated with a standing wave in the chamber.

The second burner configuration is the coaxial shear jet with gaseous methane fuel flowing in the center tube and oxygen-enriched air through the outer annular region. The inner and outer diameter dimensions are noted in chapter two. This study continues the single jet experiments described in the previous paragraph by keeping the methane Reynolds number

and the outer co-flow air constant. In addition, the oxidizer ratio of co-flow and annular flow is kept constant and monitored by sonic nozzles. The same type of acoustic forcing experiments is performed on the coaxial jet. Matching more of the properties in single and coaxial jets enables a comparison of the effect of burner configuration on dynamics of the combustion instabilities.

1.3.2 Energy and Propulsion Research Laboratory at UCLA

Somewhat similar in configuration to the AFRL experiments, at UCLA, experiments on gaseous microjet laminar diffusion flames in an acoustically resonant environment, for both single jet and coaxial jets, have been performed by Andres Vargas, as part of his Ph.D. dissertation [Vargas, 2019] as well as the current author, to analyze the combustion instability and the flame structure. These studies build on prior experiments over the years involving the combustion of liquid fuel droplets with and without nanoparticulates [Dattarajan et al., 2006, Sevilla-Esparza et al., 2014, Sevilla Esparza, 2013, Bennewitz et al., 2018]. The acoustic waveguide apparatus is a cylindrical tube with both ends enclosed with two loudspeakers generating sinusoidal signals. Speakers bounding the waveguide tube can be moved, enabling one to alter the location of pressure node or anti-node locations when an acoustic standing wave is created. The single gaseous jet port is placed at the center of the waveguide tube's geometric center. A concentric shear coaxial burner is the second configuration that is studied, where the inner tube consists of the gaseous jet methane and the outer annular flow is air, in a similar configuration to that studied at AFRL but without oxygen enrichment. The thickness of the inner tube is changed to study the self-activated shear/wake phenomena of the flames and its consequence on transition or blow-off frequencies. For both configurations, the methane Reynolds number ranges from 20 to 100. In a coaxial jet, the velocity ratio of the annular oxidizer flow to the inner fuel is matched to the study done at AFRL (R=0.05, 0.17, and 0.3). The next chapter provides further detail into the experimental setup and analyzing techniques.

1.4 POD Analysis

Snapshot Proper Orthogonal Decomposition (POD) is a data analysis algorithm used in our research group at UCLA and AFRL to study flow instability [Vargas, 2019, Plascencia Quiroz, 2021]. The importance of POD in studying turbulence was introduced by Lumley for the first time [Meyer et al., 2007, Berkooz et al., 1993]. With POD applied to temporally and spatially involving images, the mode shapes and frequencies are extracted based on the pixel intensity fluctuations. The data obtained in the course of experiments from high-speed camera imaging is used for modal decomposition and extraction of the spatial and temporal structures of the most energetic flow dynamic, essential for flow instability analysis [Schmid, 2010]. This process reveals the most dominant mode structures from dynamic couplings [Holmes et al., 2012]. POD is a linear mathematical procedure; however, it makes no linear assumption in processing data [Berkooz et al., 1993], which is why POD could resemble Fourier analysis [Berkooz et al., 1993]. Proper orthogonal modes (POMs) are used to arrange the images based on the energetic level of their pixel intensity, where pixel intensity varies with the time average [Holmes et al., 2012].

There are two main POD methods used in data analysis. The first method is snapshot POD, and the second method is single value decomposition POD. In our study, the first method of snapshot POD is implemented due to a reasonable number of frames; typically 1000 frames are used in the application of this method for each excitation condition explored. Snapshot POD was first introduced by Sirovich in 1987 [Meyer et al., 2007]. First, a single image is saved as a 2D matrix containing all the image pixel intensity values. The total number of pixel intensity values is $M \times N$. Then, the column pixel values are combined to turn the 2D matrix into a vector [Meyer et al., 2007].

$$\mathbf{D} = \begin{bmatrix} d^1 & d^2 & \cdots & d^N \end{bmatrix} = \begin{bmatrix} d_1^1 & d_1^2 & \cdots & d_1^N \\ d_2^1 & d_2^2 & \cdots & d_2^N \\ \vdots & \vdots & \vdots & \vdots \\ d_M^1 & d_M^2 & \cdots & d_M^N \end{bmatrix} \tag{1.2}$$

The covariance matrix which is used in snapshot method is created as follows (Equation 1.3):

$$\tilde{C} = D^T D \tag{1.3}$$

Using the eigenvalue problem (Equation 1.4), the eigenvectors constructing the POD modes can be extracted. The POD code in our lab is written by Andres Vargas based on the snapshot theory where a detailed mathematical description of snapshot POD analysis is included in Meyer's paper [Meyer et al., 2007]. In this study, the mean is removed prior to performing the POD.

$$\tilde{C} A^i = \lambda^i A^i \tag{1.4}$$

Where POD modes (ϕ) is:

$$\phi^i = \frac{\sum A_n^i d^n}{|| \sum A_n^i d^n ||} \tag{1.5}$$

Where A_n^i is the nth component of the eigenvector (corresponding to eigenvalue λ^i in Equation 1.4).

The results shown here correspond to a framing rate of 1000 frames per second (fps), with analysis applied throughout 0.5 s for 500 time-series shots (1000 fps is preferred over 2000 fps because additional erroneous peaks were observed with 1000 fps visible imaging). The coefficient plots are extracted to represent dynamical characteristics, similar to a phase portrait. Additionally, one can extract each mode's power spectral density (PSD) information to see frequencies associated with dominant peaks. As stated previously, POD extracts

and orders the most dominant mode structures in a data field based on energy content to highlight the most energetic dynamics of a system. Therefore, although the most energetic modes are established with POD, power spectra density (PSD) analysis is needed to reveal the frequencies associated with the modes.

CHAPTER 2

Experimental Setup and Procedures

This section provides an overview of the waveguides and the burner configurations used in the experimental setups at UCLA and AFRL. All the experiments are performed in a closed acoustic waveguide under atmospheric conditions. The acoustic waveguides used at AFRL and UCLA have similar configurations, as discussed in detail in this chapter. While AFRL's initial waveguide design is motivated by O'Connor, the configuration at UCLA has been in place for nearly two decades, and as noted earlier has been studied for liquid droplet combustion [Bennewitz et al., 2018] as well as gas phase combustion [Sim et al., 2020, Vargas, 2019, Vargas et al., 2020]. The schematic diagrams and the images used to describe the experimental setup are extracted from Miguel A. Plascencia Quiroz's Ph.D. dissertation [Plascencia Quiroz, 2021], Andres Vargas's PhD prospectus [Vargas, 2019], and Sim, et al.'s CST paper [Sim et al., 2020].

2.1 Air Force Research Laboratory (AFRL)

The AFRL studies are performed at Edwards Air Force Base (AFRL/RQR). The following sections give an overview of the experimental setup, including the atmospheric waveguide and the burner configurations. The information on the waveguide, the burners configurations, and the models are from Miguel A. Plascencia Quiroz's Ph.D. dissertation, where he performed the experiments and analysis [Plascencia Quiroz, 2021].

2.1.1 AFRL Waveguide Schematic

The acoustic waveguide used in the AFRL research facility is shown in Figure 2.1. The aluminum waveguide has dimensions of 914.4 mm x 355.6 mm x 108.0 mm. The length of the waveguide has a direct effect on altering the acoustic resonance. Therefore, sectional pieces are used to accommodate the length modification for the waveguide. As shown, the burner is placed at the geometric center of the waveguide. The detailed burner configuration is discussed in the next section.

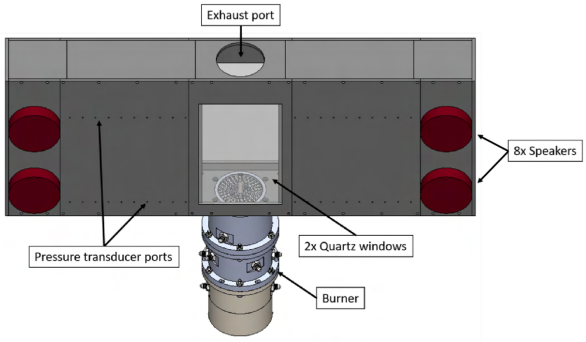

Figure 2.1: CAD assembly illustrating details of the acoustic channel and burner used in the AFRL research facility [Plascencia Quiroz, 2021].

Two windows (165.1 mm x 279.4 mm x 6.35 mm) are placed in the middle of the waveguide for flame and jet imaging. An ignition port with a diameter of 25.4 mm is located at the bottom of the waveguide. The port above the burner with a diameter of 88.9 mm is the exhaust exit. Pressure transducers are placed at 6.35 mm and 152.4 mm from the bottom of the waveguide. Four speakers are mounted at each end of the waveguide at 88.9 mm from the top/bottom and 50.8 mm from the sides for acoustic forcing. Thus, there is a total of eight speakers used in the channel [Plascencia Quiroz, 2021].

2.1.2 AFRL Waveguide Characteristics

Waveguide's design goal is to produce a maximum acoustically resonant pressure perturbation. Equation 2.1 represents the resonance frequency in a rectangular cavity, in which c is the speed of sound, $n_{x,y,z}$ are integers representing various modes in the x, y, and z direction; L_x the transverse length; L_y the height, and L_z the width of the waveguide. The odd n values correspond to pressure node (PN) or velocity antinode resonances, and the even integers are related to the pressure anti-node (PAN) or velocity node conditions at the center of the waveguide. By definition, when the speakers are in phase, there is a pressure anti-node (PAN) standing wave, which translates to a velocity node at the burner's location. In contrast, when the speakers are operated out of phase, there is a pressure node (PN) at the waveguide center, corresponding to a maximum in the velocity perturbation (velocity anti-node) at the exit of the burner.

$$f_a = c\sqrt{(\frac{n_x}{2L_x})^2 + (\frac{n_y}{2L_y})^2 + (\frac{n_z}{2L_z})^2} \tag{2.1}$$

Since the waveguides in question are shown to be effectively one dimensional, based on the size and verification of predicted modes [Plascencia Quiroz, 2021], n_y and n_z are effectively set to zero. Applying the 1D restriction on Equation 2.1, the following simplified equation is achieved to calculate the theoretical acoustic frequency (Equation 2.2).

$$f_a = c(\frac{n_x}{2L_x}) \tag{2.2}$$

Based on the length of the waveguide, 27.94 cm, and the estimated speed of sound based on atmospheric conditions, the possible resonant frequencies range of the speakers lie in the range of $200 - 5,000$ Hz, according to the manufacturer. As noted above, the flow in the waveguide is thought to be acoustically compact since the characteristic length scale of the flow (injector diameter) is much smaller than the transverse acoustic wavelength, and this is verified in the present experiments and analysis. Table 2.1 summarizes the

attained frequencies experimentally, theoretically as, assuming essentially 1D flow, well as using the simulation software COMSOL with a full three-dimensional acoutic simulation [Plascencia Quiroz, 2021]. With COMSOL, the three-dimensional model of the waveguide is incorporated into the code to determine computationally the various acoustic modes. The acoustic mode shapes are resolved with the use of the COMSOL finite element solver and the Helmholtz equation. The COMSOL application details are included in Miguel A. Plascencia Quiroz's Ph.D. dissertation [Plascencia Quiroz, 2021].

Table 2.1: Theoretical, computational, and experimental resonant frequencies and wavelengths [Plascencia Quiroz, 2021].

Transverse Waveguide Resonance ($n_{y,z} = 0$)							
		1D Theoretical		3D COMSOL		Experimental	
n_x	$L_x[cm]$	$f_{a,th}$ [Hz]	λ_{th} [cm]	$f_{a,comsol}$	λ_{comsol} [cm]	$f_{a,exp}$	λ_{exp} [cm]
1	91.44	188	1.83	189	1.8	-	-
2	91.44	375	0.91	363	0.94	375	0.92
3	91.44	563	0.61	567	0.6	571	0.6
4	91.44	750	0.46	750	0.46	775	0.44
5	91.44	938	0.37	941	0.36	942	0.36
6	91.44	1125	0.3	1116	0.31	1150	0.3
7	91.44	1313	0.26	1318	0.26	1314	0.26
8	91.44	1500	0.23	-	-	-	-
9	91.44	1688	0.2	1693	0.2	-	-
10	91.44	1876	0.18	-	-	-	-
11	91.44	2063	0.17	2066	0.17	-	-

For three of the odd transverse mode values (corresponding to $n_x = 3, 5, 7$), pressure node frequencies of 571 Hz, 942 Hz, and 1314 Hz are determined experimentally at AFRL, measured via conducting a frequency sweep in the waveguide for speakers operating out

of phase and measuring peaks in pressure responses via embedded pressure transducers. The first odd mode ($n_x = 1$) is outside of the speakers' frequency range, which is why an experimental value is not noted in Table 2.1. Otherwise, the correspondence between the experimentally measured resonant frequencies and the 1D theoretical and 3D computational values is quite good. Similarly, using the first three even modes ($n_x = 2, 4, 6$), experimentally measured frequency values of 375 Hz, 775 Hz, and 1150 Hz are achieved for the pressure anti-node condition at the geometric center. Here, too, the experimental measurements are consistent with the COMSOL 3D model and the 1D theoretical estimated values. Note that the experimental measurement values differ once the burner and the flame are included inside the waveguide, since of course the temperature in the waveguide is altered and the presence of the flame alters the acoustic field. Moreover, the burner tubes themselves have natural resonances which the applied frequencies should avoid, if possible. Hence the following frequencies were used for pressure node (PN) cases: 581 Hz (approximately $n = 3$), 1348 Hz (approximately $n = 7$), and 2065 Hz (approximately $n = 11$). Similarly, the forcing frequencies were used for pressure anti-node (PAN) cases: 360 Hz (approximately $n = 2$), 775 Hz (approximately $n = 4$), and 1150 Hz ($n = 6$).

2.1.3 AFRL Burner Configurations

At AFRL, two alternative burner configurations are incorporated in the acoustically coupled jet combustion experiments. In this following section, each structure is summarized. The first one consists of a single burner with co-flow, as seen in Figure 2.2. The singlet jet has a center tube with an inner diameter of 4 mm and a post-thickness of 0.36 mm. The center tube is surrounded by another larger tube with an outer diameter of 88.9 mm. The two tubes are concentric and have a fully developed turbulent flow at the exit. Equation 2.3 calculates the entrance length L for a fully developed turbulent flow. The Re is the turbulent Reynolds number of the methane inside the inner tube, and D is the inner tube's exit diameter.

$$L/D = 4.4Re^{(1/6)} \tag{2.3}$$

Based on Equation 2.3, in order to have a fully developed turbulent methane with a Reynolds number of $5,300$, the length of the inner tube and the outer tube must respectively be 30.5 cm and 25.4 cm. As shown in Figure 2.2, the co-flow regime is only 16.84 cm, where 6.05 cm of that is filled with spheres. At the exit of the burner, a honeycomb with a thickness of 2.54 cm and 88.00 mm diameter is placed. The purpose of the co-flow is to reduce the entrainment and re-circulation flow in the vicinity of the jet. The oxygen concentration (60 percent N_2 + 40 percent O_2) is selected to keep the flame anchored at a cow-flow velocity of 1 m/s.

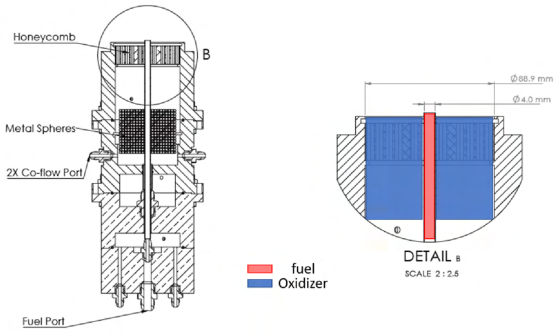

Figure 2.2: Schematic of the burner as a single jet with co-flow used in the AFRL research facility [Plascencia Quiroz, 2021].

The second configuration is the coaxial jet (see Figure 2.3). The coaxial jet has a similar configuration to a single jet with the addition of an annular oxidizer tube. The center fuel tube has an inner diameter of 4 mm with a post thickness of 0.36 mm. The diameter of the annular tube, is 11.23 mm with a post thickness of 0.36 mm. Lastly, similar to the single jet, the tubes are surrounded by a co-flow tube with an outer diameter of 88.9 mm. The co-flow air velocity and concentration are kept constant and are the same as the single jet configuration. The Reynolds number of methane is kept constant in both designs, and the

only variant is the annular oxidizer velocity to achieve different velocity ratios for the coaxial jet. The velocity ratio of the annular oxidizer to the inner methane is called R. At AFRL, velocity ratios of 0.05, 0.17, and 0.3 are studied while the methane Reynolds number is kept constant at $5,300$. Thus, the annular flow velocity ranges from 1 m/s to 6.5 m/s, while the co-flow is held at a constant velocity of 1 m/s.

High-speed Schlieren and OH^* chemiluminescence are the imaging methods used at AFRL to capture the visible and invisible flame response to external acoustic excitation [Plascencia Quiroz, 2021]. OH^* chemiluminescence imaging uses the flame intensity to identify the shape and size of a reaction zone and to study the temporal coupling between the flame and the external acoustic forcing. This type of imaging works with capturing the chemiluminescence of an electrically excited hydroxyl radical, OH^*. OH^* chemiluminescence images are also used to study the heat release of the flame, flame height, and flame lift-off distance.

The high-speed schlieren method explores the imperceptible density gradient that conveys information on the naturally occurring flame dynamics and shear/wake-like flame responses under acoustic forcing. The captured schlieren images of an unforced turbulent jet at AFRL indicate that the inner core of the flame is naturally unstable [Plascencia Quiroz, 2021]. Thus, the schlieren method is especially useful in studying the coaxial jets to analyze the interaction of the core methane and outer air flows to detect naturally occurring shear/wake patterns and their effect on the flame structure. Phantom research camera and Nikon v2511 lens were the optics used for high-speed Schlieren imaging at AFRL [Plascencia Quiroz, 2021]. Although Schlieren imaging identifies the naturally occurring flame dynamics, it is most useful for turbulent regimes. Our research group (EPRL) used visible imaging to study the flame dynamics in a coaxial flow under a laminar jet diffusion flame.

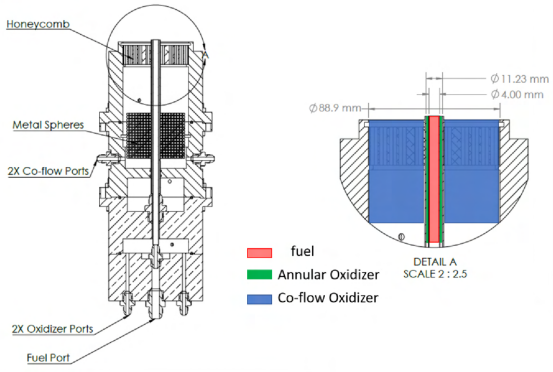

Figure 2.3: Schematic of burner as a coaxial jet with co-flow used in the AFRL research facility [Plascencia Quiroz, 2021].

2.2 Energy and Propulsion Research Laboratory at UCLA

2.2.1 UCLA Waveguide Schematic

In our research group at the Energy and Propulsion Research Laboratory at UCLA, the following experimental setup (Figure 2.4) has been used over the years. The closed cylindrical waveguide operates at atmospheric conditions with two speakers mounted at each end. As seen in Figure 2.4, the front and the back windows at the geometric center of the waveguide are for optical accessibility of a high-speed camera as well as a CCD camera operating in the UV for OH^* chemiluminescence imaging of the burner and the flame. Fig. 2.4 is the overall experimental setup of the combustion instability tests. This includes a high-speed imaging camera, a UV camera for OH^* chemiluminescence imaging (though results are not shown here), and the waveguide mounted on the table, with a Halogen lamp at the back window of the waveguide used to image the burner's position.

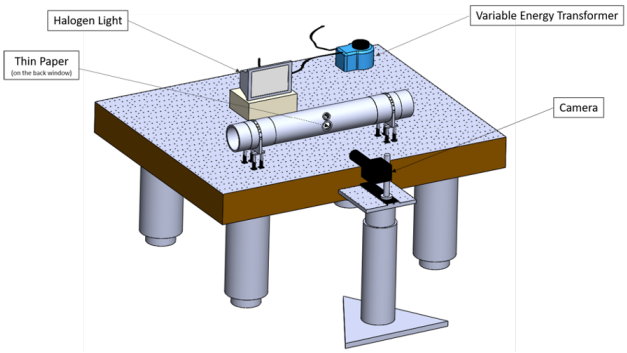

Figure 2.4: CAD assembly illustrating details of the acoustic waveguide and the experimental setup used in our research group at the Energy and Propulsion Research Laboratory (EPRL) at UCLA.

The waveguide has an inner diameter of 11.43 cm and an outer diameter of 12.7 cm. The length of the waveguide is adjustable by adding an extension. The maximum achievable distance between the speakers is 61 cm, and the lowest length is 31 cm. The waveguide is designed such that the speakers could be moved longitudinally, with the distance between them fixed. This enabled the position of the pressure node or pressure antinode to be moved relative to the burner, which was fixed at the geometric center of the tube. Table 2.2 in the next section summarizes the experimental and theoretical frequency and wavelength for each attainable size. The optical window for imaging has an inner diameter of 3.14 cm to capture the burner. A more detailed setup of the experiments is included in Figure 2.5. Similar to AFRL, both single jet and coaxial jets have been experimented with in this study. In addition, methane tube with different wall thickness is tested to study the effect of the shear layer/wake-like dynamics on flame stability. A more detailed description of the burner is discussed in the next section.

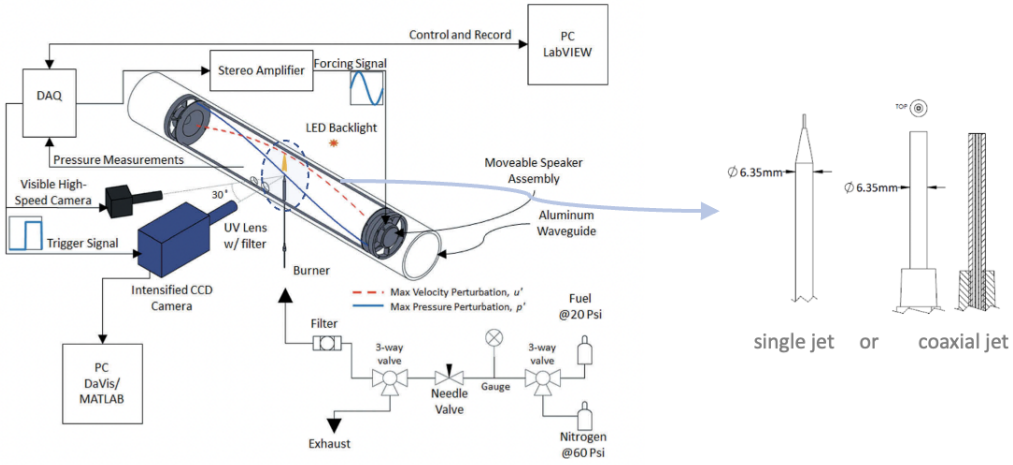

Figure 2.5: CAD assembly illustrating details of the acoustic channel for the single and coaxial jet used in our research group at the Energy and Propulsion Research Laboratory (EPRL) at UCLA adapted from Sims et al. [Sim et al., 2020].

A sinusoidal signal is generated through the LabView Software (Figure 2.5) to create one-dimensional planar standing waves at the waveguide. First, the signal's initial frequency and voltage are adjusted to match the required oscillatory pressure amplitudes. Then, the speakers are operated out of phase by inverting the speaker's polarity connection. The standing wave that forms creates a velocity antinode or pressure node at the geometric center of the distance between the two speakers. Moving the speakers but fixing the distance between them enables the burner to be situated at one side or the other of the PN. A pressure transducer (XCE-093-50D, Kulite) is placed at the closest pressure antinode to the PN to measure the maximum oscillatory pressure amplitude. A second transducer is placed at the geometric center of the waveguide, which is the jet's location, to determine the local oscillatory pressure. The script used in the LabView used a control feedback loop (written by Andres Vargas) to use a proper voltage amplitude during each experiment.

2.2.2 UCLA Waveguide Characteristics

For the pressure node (PN) condition at the center of the waveguide, the following forcing frequencies are found experimentally to correspond to the pressure node conditions at the geometric center: 332 Hz, 586 Hz, and 898 Hz (see Table 2.2), corresponding to modes $n = 1$, 3, and 5 in Equation 2.2. In this study, only the forcing frequency of 332 Hz with a speaker distance of 61 cm is explored since it was found in earlier droplet combustion studies to have the most significant influence on burning systems. Similar to the AFRL waveguide, Equation 2.2 is used to estimate the theoretical frequency of 1D standing waves based on the speed of sound c and the length between the two speakers L. To have a symmetrical acoustic pressure profile in the vicinity of the pressure node, a signal from LabView software is outputted to the speaker while keeping a constant voltage. Then, the speakers are shifted with trial and error until a symmetrical profile is achieved.

Table 2.2: Theoretical and experimental resonant frequencies and wavelengths from Bennewitz et al. [Bennewitz et al., 2018].

Speakers (180 degrees out of phase) with Pressure Node at x=0 cm					
		1D Theoretical		Experimental	
n_x	$L_x[cm]$	$f_{a,th}$ [Hz]	λ_{th} [cm]	$f_{a,exp}$ [Hz]	λ_{exp} [cm]
1	61	281	122	332	103
1	31	553	62	586	58.5
3	61	843	40.7	898	38.2

As seen in Table 2.2, the 1D theoretical estimation and the experimental values of the forcing resonance modes compare reasonably well. As with the AFRL experiments, we use the experimental data for higher accuracy. The waveguide characterization used in our research group is similar to the AFRL study explained in section 2.1.2, where a frequency sweep identifies the resonant modes. The only difference is that our group only places the

pressure node (PN) in the vicinity of the burner and not the pressure anti-node (PAN).

The local oscillatory pressure p' and velocity perturbation u' are estimated from the maximum pressure perturbation p'_{max} using the one-dimensional planar wave equation. The equations below are the momentum linearized equations where p'_{max} is the oscillatory pressure amplitude at the pressure anti-node (PAN) [Bennewitz et al., 2018].

$$p'(x,t) = Re(-p'_{max} sin(\frac{2\pi x}{\lambda}) exp(iwt)) \tag{2.4}$$

$$u'(x,t) = Re(-i\frac{p'_{max}}{\rho_o c} cos(\frac{2\pi x}{\lambda}) exp(iwt)) \tag{2.5}$$

Equations 2.4 and 2.5 are used in chapter three to calculate the oscillatory pressure and velocity from the pressure transducer measurements. Additionally, as noted in Bennewitz et al. [Bennewitz et al., 2018], an actual hot-wire has been placed at the velocity anti-node location in the waveguide to verify the oscillatory velocity profile.

2.2.3 UCLA Burner Configurations

Our research group at UCLA has several alternative configurations to study laminar microjet instability under acoustic forcing. Two of the studied configurations are single and coaxial jets, respectively (see Figures 2.6 and 2.7). The main difference between the AFRL and UCLA EPRL burner configurations is the outer low-velocity co-flow section in AFRL design which is a part of the UCLA EPRL setup. In this section, the sizings of the jets are reviewed. The single jet consisted of a central methane tube with an outer diameter of 0.794 mm and a port with an outer diameter of 6.35 mm (see Figure 2.6). The purpose of the port is to keep the fuel port at a stable position during the experiments. The single laminar jet is tested under acoustic forcing at 332 Hz with jet inner diameter-based Reynolds numbers ranging from 20 to 100.

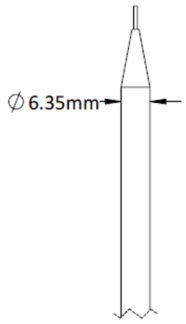

Figure 2.6: Schematic of the burner as a single jet outline used in our research group at the Energy and Propulsion Research Laboratory (EPRL) at UCLA.

The coaxial burner is tested inside the waveguide as the second alternative configuration (see Figure 2.7). The annular burner has a constant outer diameter of 6.35 mm with a wall thickness of 1.6 mm (inner diameter of 3.2 mm). The annular tube is kept constant throughout the experiment, with the exact dimensions while the oxidizer (air) flow rate is varied. The central port has a constant outer diameter of 1.6 mm. Two different wall thicknesses are tested for the central port. The thicker tube has a thickness of 0.29 mm with an inner diameter of 1.0 mm, while the thinner tube has a wall thickness of 0.5 mm with an inner diameter of 0.5 mm. Two different wall thicknesses are studied to analyze the burner's cross-sectional thickness effect on the flame instability.

In coaxial jet experiments, the flow rate of the center port (methane) is kept constant for both wall thickness configurations while the annular oxidizer's flow rate is varied. Therefore, the velocity ratio R of the oxidizer (annular flow) to the methane (central tube) is of our interest. We have tested velocity ratios of 0.11, 0.33, and 1 to see the effect of R in generating shear/wake-like behaviors in the flame. Similarly, at AFRL, velocity ratios of 0.05, 0.17 and 0.3 are tested, which is comparable to our work at UCLA. This way, the laminar and turbulent coaxial jets under acoustic forcing from both research groups can be compared to each other (see chapter 3).

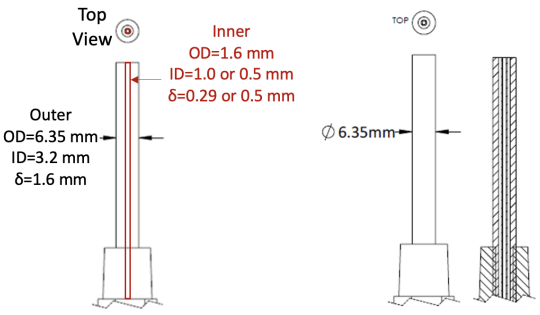

Figure 2.7: Schematic of the burner as a coaxial jet outline used in our research group at the Energy and Propulsion Research Laboratory (EPRL) at UCLA.

CHAPTER 3

Result Comparison

3.1 Single Jet

While both AFRL and our research group at UCLA EPRL study the flame response to external acoustic forcing, they diverge in several ways in the burner configuration, flow regime, and the relative applied forcing amplitudes. Therefore, the initial result comparison starts with analyzing the cross-sectional geometry of the two burners used in the single jet experiments, as shown in Figure 3.1. Note that a detailed description of the difference between the two burners' geometry is discussed in chapter two of this thesis.

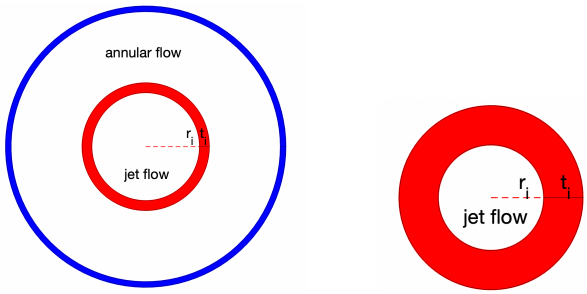

(a) (b)

Figure 3.1: **Single Jet**: Burners' cross sectional schematics. (a) AFRL's burner configuration with a center jet (inner diameter of 4.0 mm, post thickness of 0.36 mm) surrounded by an annular flow section (outer diameter of 88.9 mm) [Plascencia Quiroz, 2021]. (b) UCLA EPRL's burner schematic with an inner diameter of 0.457 mm and an outer diameter of 0.794 mm [Sim et al., 2020].

To nondimensionalize the geometry of the jet, the ratio of t_i/r_i is of interest, where t_i is the jet tube's wall thickness, and the r_i is the inner radius of the jet burner (see Figure 3.1). In Table 3.1, some of the key differences between the two experimental setups for the single jet are listed. The thickness to inner radius ratio, t_i/r_i, of AFRL and UCLA EPRL are respectively 0.18 and 0.74. The nondimensionalized geometry ratio of the laminar burner is four times larger than the turbulent burner. A higher flow rate is necessary for a turbulent flow; hence, the burner has a larger inner radius leading to a smaller thickness to radius ratio. Comparing the post thicknesses solely, it is evident that the AFRL turbulent burner has a wall thickness of about twice that of the UCLA-based experiments with laminar flow. The wall thickness of the injector tube is crucial in the heat re-circulation and the shape of the flame, which is directly related to the flame's sustainability.

Table 3.1: AFRL and UCLA EPRL experimental setup comparison [Plascencia Quiroz, 2021, Sim et al., 2020].

	AFRL	UCLA EPRL
Imaging	Schlieren and OH* Chemiluminescence	High-Speed Visible Imaging
Flow Regime	Turbulent (Re $\approx$ 5300)	Laminar (Re $\approx$ 65)
Inner Radius (r_i) [mm]	2.00	0.23
Post Thickness (t_i) [mm]	0.36	0.17
t_i/r_i	0.18	0.74

The post thickness of the burner is a more important topic in the coaxial jet study since it can dictate the shear or wake-like behavior of the air and methane at the contact point [Megerian et al., 2007, De B. Alves et al., 2008]. Based on our prior knowledge of the effect of wall thickness on the flow field [Norton and Vlachos, 2003], the thinner wall has a better heat transfer and preheating ability, which results in relatively complete combustion with less soot formation, leading to flame's increased sustainability under acoustic forcing. But such comparison would be appropriate in comparing the same flow regimes and not turbulent

versus laminar. Hence since the two flow regimes are vastly different, the post thickness and the inner radius are not explored in detail for the single jet between the two cases.

3.1.1 Pressure Node (PN) Forcing

Flame structures with relatively axisymmetric oscillatory shapes are selected to compare acoustically coupled combustion under laminar and turbulent conditions. Turbulent jet flow in the AFRL experiments with 581 Hz forcing frequency at an excitation amplitude at the nearest PAN in the waveguide of $p'_{max} = 600$ Pa (e.g., at the pressure node or PN) and laminar fuel jets in the UCLA experiments with 332 Hz forcing frequency at an excitation amplitude of $p'_{max} = 100$ Pa (i.e., the pressure perturbation at the closest PAN, where the flame is located near the but not precisely at the PN), have symmetrical flame structures (see Figure 3.2) at relatively low level excitation. Although both flames are at or near the pressure node, the ratio of the local velocity at the burner location to the jet velocity is an important aspect that must be considered while comparing the results. The turbulent burner has a jet velocity of 24 m/s with a velocity excitation amplitude estimated from the pressure perturbation of 1.9 m/s, while the laminar burner has a jet velocity of 2.4 m/s and estimated velocity excitation amplitude of 0.24 m/s [Plascencia Quiroz, 2021, Sim et al., 2020].

The ratio of local perturbation velocity u' and jet velocity U_j helps to understand the effect of velocity perturbation at the vicinity of each burner location shown in Figure 3.2. For the turbulent flame, the ratio is 1.9 m/s (u') over 24 m/s (U_j), which yields value of 0.079 [Plascencia Quiroz, 2021]. Similarly, the laminar flow has a ratio of 0.24 m/s (u') over 2.4 m/s (U_j) with a perturbation velocity ratio of 0.1 [Sim et al., 2020]. A higher ratio indicates a more severe flame response as a result of excitation. The turbulent jet has a high jet velocity compared to the local velocity perturbation at the vicinity of the burner, but its ratio of u'/U_j is not much lower than that for the UCLA experiments, and hence its flame response consists of a low level flame oscillation with essentially symmetric structural

alterations, as shown in Figure 3.2. While the excitation amplitude for the UCLA experiments in Figure 3.2(b) is at the lowest level explored [Sim et al., 2020], the amplitude for the AFRL experiments is the maximum attainable level, yet the response is clearly far from any transition point of sustained oscillatory combustion (SOC) to periodic liftoff and reignition (PLOR) observed in flame structures in the UCLA experiments [Sim et al., 2020] at higher amplitudes of excitation. Hence while the raw amplitude of pressure perturbation for the AFRL experiments is a factor of 6 larger than that for the UCLA experiments in this figure, its relatively low velocity perturbation suggests that the AFRL experiments cannot attain PLOR in the current state, which is in fact what was observed [Plascencia Quiroz, 2021]. Nevertheless, modal decomposition tools developed at UCLA enabled helpful application in the AFRL experiments, and comparisons could be made at low level excitation conditions.

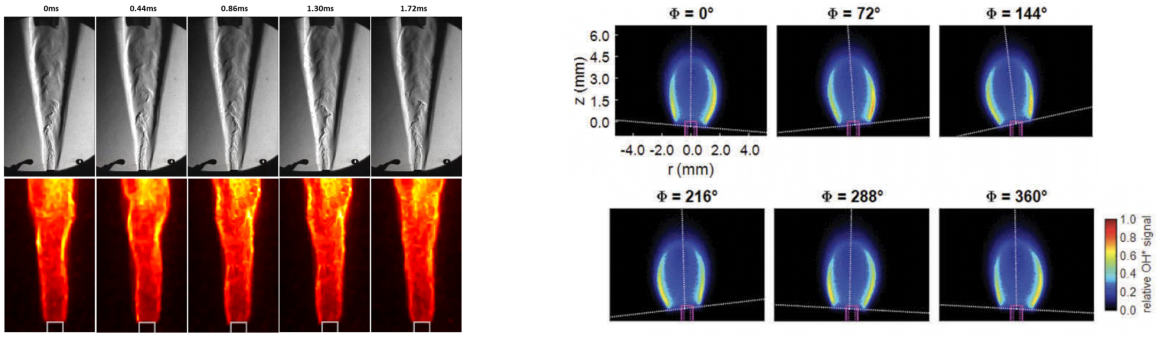

(a) (b)

Figure 3.2: **Single Jet**: Sequence of images over time/phase. (a) AFRL's Schlieren and and OH* chemiluminescence images for 581 Hz excitation at an amplitude of $p'_{max} = 600$ Pa ($u' = 1.9$ m/s) at a PN with $U_j = 24$ m/s ($u'/U_j = 0.079$) [Plascencia Quiroz, 2021]. (b) UCLA EPRL's phase-locked OH* chemiluminescence images for $p'_{max} = 332$ Hz excitation at an amplitude of 100 Pa ($u' = 0.24$ m/s) near a PN with $U_j = 2.4$ m/s ($u'/U_j = 0.1$) [Sim et al., 2020].

Spectral analysis of each of the temporal coefficients for the laminar and turbulent flames can be obtained from the POD analysis, which can be instructive in understanding correspondence to flame dynamics. These are plotted in a power spectral density (PSD) format shown in Figure 3.3. The first two POM modes peak at 581 Hz, which is the applied forcing frequency, and with several higher harmonics of 581 Hz generated as well. Higher POM modes with lower energy content (3 and 4) do not indicate clear peaks, with more noisy spectral content. Similarly for the UCLA experiments in Figure 3.3(b), a clear peak at the applied excitation frequency 332 Hz is seen in the PSD plot for POM mode 1. Both PSD results suggest the locking-in of the oscillating flame under the applied acoustic forcing. In the absence of external excitation, neither the AFRL nor UCLA experiments showed natural flame instabilities for the single jet [Plascencia Quiroz, 2021, Sim et al., 2020], so for these conditions it was not possible to explore in rigorous detail shear layer instability phenomena such as convective instability or lock-in characteristics.

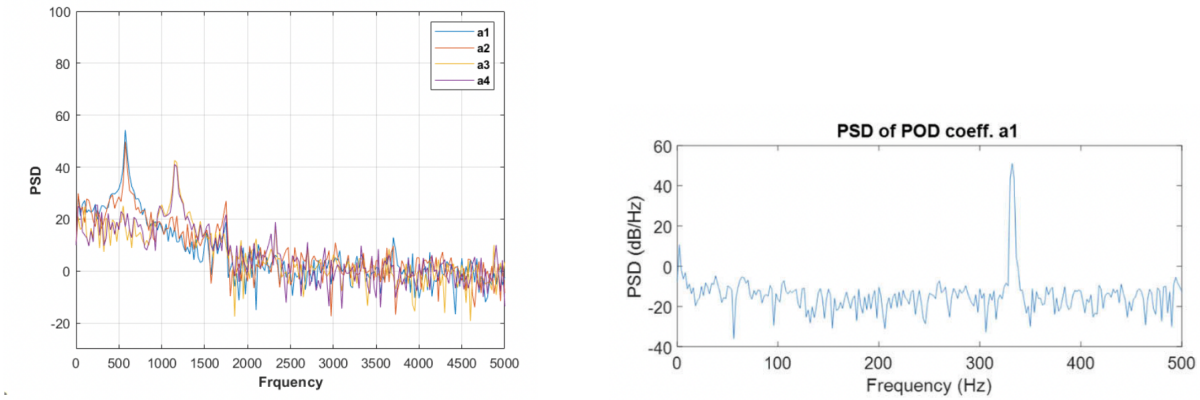

(a) (b)

Figure 3.3: **Single Jet**: POD analysis results. (a) AFRL's power spectral density associated with the first four POD modes for 581 Hz excitation at $u'/U_j = 0.079$ [Plascencia Quiroz, 2021]. (b) UCLA EPRL's power spectral density associated with the four POD modes for 332 Hz excitation at an amplitude of $u'/U_j = 0.1$ [Sim et al., 2020].

The POD mode coefficients for the first four modes of turbulent and laminar diffusion flames subjected to forcing at or near the PN are shown in Figure 3.4. The plotted POD modes are ordered according to the percentage of the energy content. Figure 3.4(a) includes the four highest energy percentages exposed to an excitation amplitude of $u^{'} = 1.9$ m/s based on pixel intensity variations [Plascencia Quiroz, 2021]. The four highest-ranked POD structures in Figure 3.4(b) correspond to visible imaging of the laminar flame under a low excitation amplitude of 100 Pa [Sim et al., 2020]. In both cases, the first Proper Orthogonal Mode (POM1) of course has by far the highest energy level with a relatively symmetric structure concerning the burner axis. Other modes in both cases also display a relatively symmetric flame structure, though the percentage energy content of these higher modes for the AFRL experiments tends to be larger than for the UCLA experiments. Based on observed transitions in POD modes for the UCLA experiments at higher amplitude forcing [Sim et al., 2020], the observations in Figure 3.4 suggest that the dynamical conditions for the AFRL experiments may be slightly closer to a transition in flame response, with possible liftoff, than the UCLA experimental result shown in Figure 3.4(b). For higher amplitude UCLA excitation conditions, PLOR was routinely observed in the run-up to full scale flame blowoff (BO). Thus, despite the minor difference in the energy content in Figure 3.4, both cases demonstrate a similar pattern overall.

Results such as those in Figure 3.2 enable one to plot the POD mode coefficients against each other, and this can be used to study the flame dynamics (see Figure 3.5). The plotted mode coefficients against each other also investigate the flame dynamics dominated by a linear combination of the modes. Such a linear dominance of the mode coefficients indicates periodic wavelike behavior. Figure 3.5(a) is the turbulent flame phase portraits of the AFRL single jet with Reynolds of 5300, and Figure 3.5(b) is the laminar flame (UCLA EPRL) POD subjected to acoustic forcing with a Reynolds number of 65 [Plascencia Quiroz, 2021, Sim et al., 2020]. Both phase portraits have similar patterns and shapes even though they lay on two vastly different flow regimes. For example, the coefficients a1 vs. a2 have oval shapes,

indicating periodicity for both laminar and turbulent flames subjected to 600 Pa and 100 Pa excitation forcing, respectively (Figure 3.5).

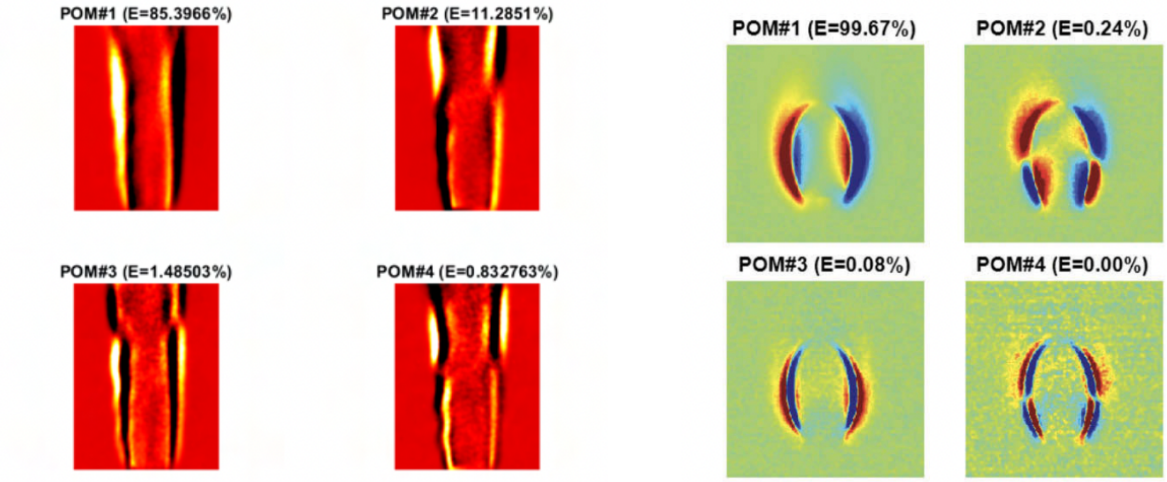

(a) (b)

Figure 3.4: **Single Jet**: POD plots. (a) AFRL's first four POD spatial modes with associated percentage of energetic content analysis results for 581 Hz excitation at an amplitude of $p'_{max} = 600$ Pa ($u'/U_j = 0.079$) [Plascencia Quiroz, 2021]. (b) UCLA EPRL's first four POD spatial modes extracted from visible imaging with associated percentage of energetic content analysis results for 332 Hz excitation at an amplitude of $p'_{max} = 100$ Pa ($u'/U_j = 0.1$) [Sim et al., 2020].

The ovular shape of the first two modes plotted against each other indicates a periodic traveling wave [Sim et al., 2020]. For example, the mode plot for a1 vs. a2 for the turbulent flame in Figure 3.5(a) is nearly circular, while a1 vs. a2 for the laminar flame in Figure 3.5(b) has an oval shape. The oval shape suggests an energy content difference between the two modes, while a more circular shape suggests a somewhat closer energy content between the two modes consistent with Figure 3.4. The rest of the phase portraits have a lower energy content but still show symmetric patterns and similarities between the single jets at different Reynolds numbers, suggesting similar dynamical characteristics and signatures.

The symmetric phase portraits for the UCLA configuration in Figure 3.5(b) began to become more skewed and asymmetric when the amplitude of excitation was increased. For example, in Figures 3.6(a) and 3.6(b), at excitation amplitudes of 175 Pa and 180 Pa, respectively, the phase portraits are observed to change significantly as compared to Figure 3.5(b). For the case of 175 Pa excitation, the flame still exhibits SOC, but it is deflected in the bulk due to its being situated near but not at the PN. For the case of 200 Pa, periodic liftoff and reattachment (PLOR) has begun to take place, and there is an additional timescale in the flow (the period associated with the liftoff and reattachment), which creates the smearing of the path in the phase portrait. For excitation at $p'_{max} = 220$ Pa, full-scale flame blow-off (BO) or extinction was observed after a few seconds of exposure to the acoustic perturbations. One does not see such alterations in the AFRL-based flame experiments because the maximum amplitude of excitation cannot create a local velocity perturbation much higher than that resulting in the symmetric phase portraits shown in Figure 3.5(a).

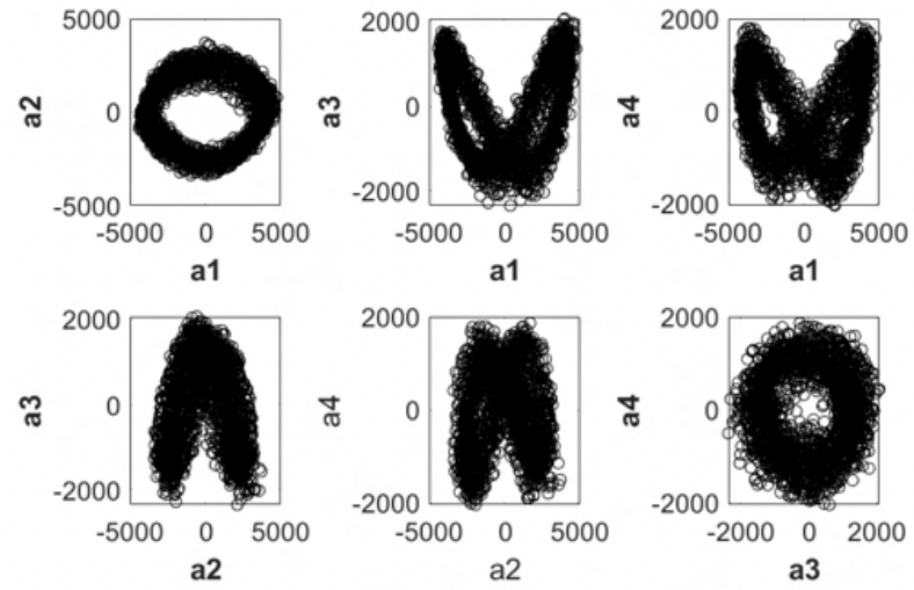

(a)

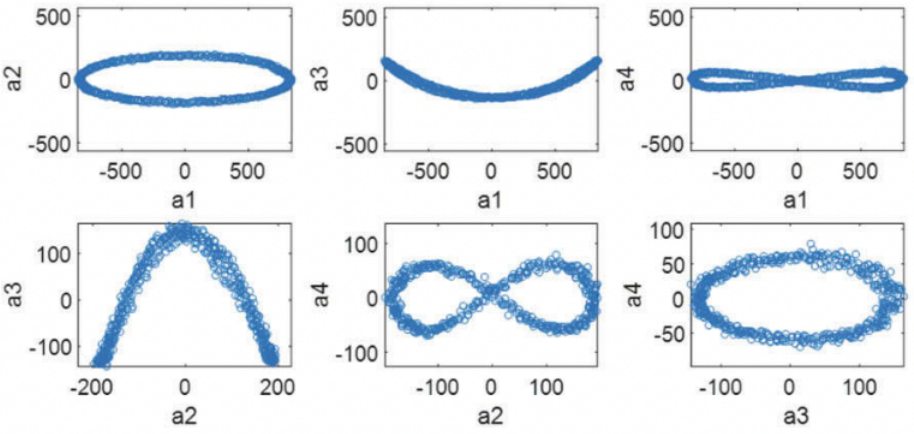

(b)

Figure 3.5: **Single Jet**: POD plots. (a) AFRL's POD mode coefficients plotted against one another for the first four modes for 581 Hz excitation at an amplitude of $u'/U_j = 0.079$ [Plascencia Quiroz, 2021]. (b) UCLA EPRL's POD mode coefficients plotted against one another for the first four modes for 332 Hz excitation at an amplitude of $u'/U_j = 0.1$ [Sim et al., 2020].

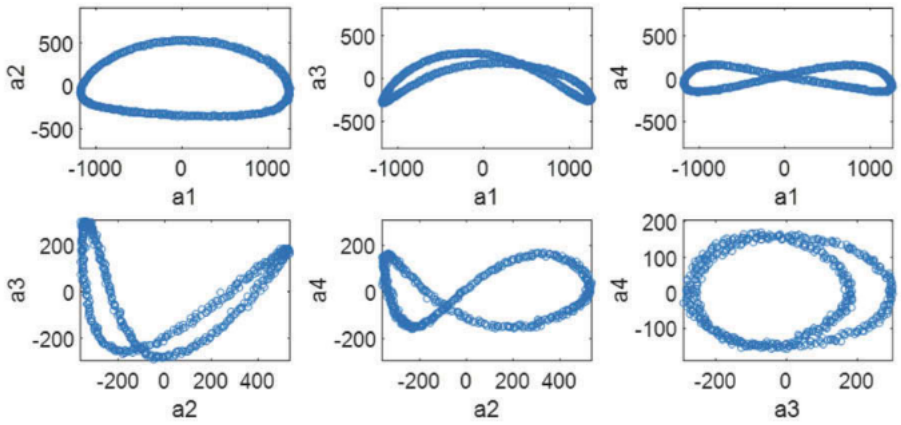

(a)

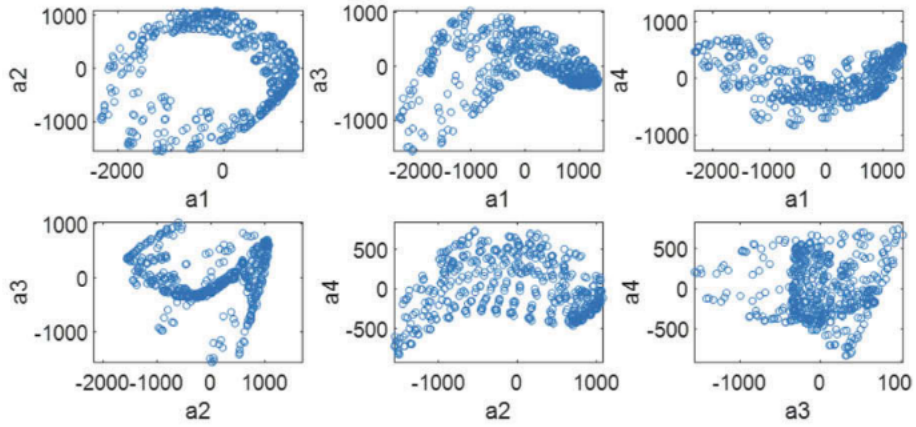

(b)

Figure 3.6: **Single Jet**: POD plots. (a) UCLA EPRL's POD mode coefficients plotted against one another for the first four modes for 332 Hz excitation at an amplitude of 175 Pa, corresponding to $u'/U_{jet} = 0.17$ [Sim et al., 2020]. (b) UCLA EPRL's POD mode coefficients plotted against one another for the first four modes for 332 Hz excitation at an amplitude of 180 Pa, corresponding to $u'/U_{jet} = 0.18$ [Sim et al., 2020].

Despite the fact that the AFRL configuration was not able to achieve high enough excitation levels to explore phenomena observed in transition to PLOR, there were many similarities between the two laminar and turbulent flames under the pressure node (PN) acoustic forcing conditions. Therefore, one can attempt to relate the trends in the transition points for the laminar flame to the turbulent one. Based on the recently performed experiments at UCLA EPRL (with Andres Vargas), transition points based on the local pressure perturbation p'_{local} for the laminar single jet flame may be plotted for each of the Reynolds numbers ranging from 20 to 100 as in Figure 3.7. Shown are transitions points for both periodic lift off and reattachment (PLOR) and full blow off (BO) of the microjet diffusion flame.

Per linear fitting of the transition points, the following equations are generated from experimental determination of the local velocity perturbation amplitude associated with PLOR ($u'_{PLOR} = 0.000705 * Re + 0.431330$) and BO ($u'_{BO} = 0.002257 * Re + 0.412940$). One can similarly determine the local pressure perturbations associated with these criteria. These laminar linear relations could potentially enable prediction of the turbulent regime. Based on the similarities of the dynamics of the reactive jets in the two flow regimes, continued linearity in the transitional/turbulent regime could be a reasonable assumption. However, to verify this theory, further experiments at AFRL are necessary.

The local velocity perturbation equations described above can be used to estimate the local velocity needed for a turbulent flame's transitional response. The local velocities necessary for a flame with Reynolds number $5,300$ to transition from SOC to PLOR and PLOR to BO are 4.2 m/s and 12.4 m/s, respectively. In the AFRL experiments with results shown in Figures 3.2-3.5, the applied local velocity forcing at the pressure node is only 1.9 m/s, which was the maximum attainable with the present AFRL configuration. This theory could be explored in future work by the research group at AFRL for confirmation.

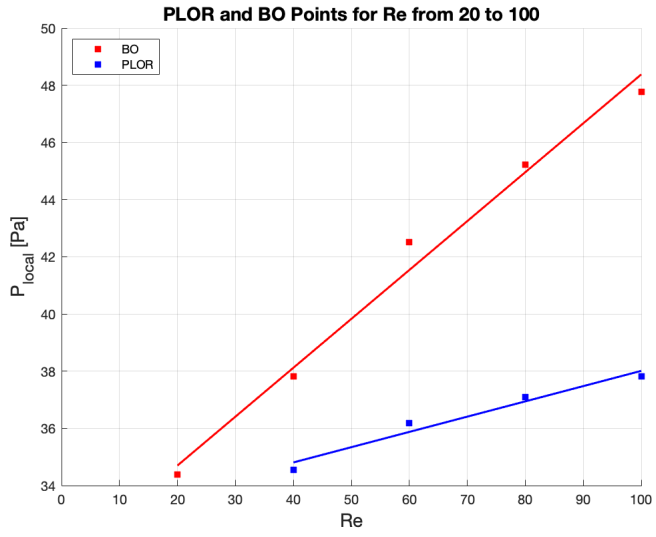

(a)

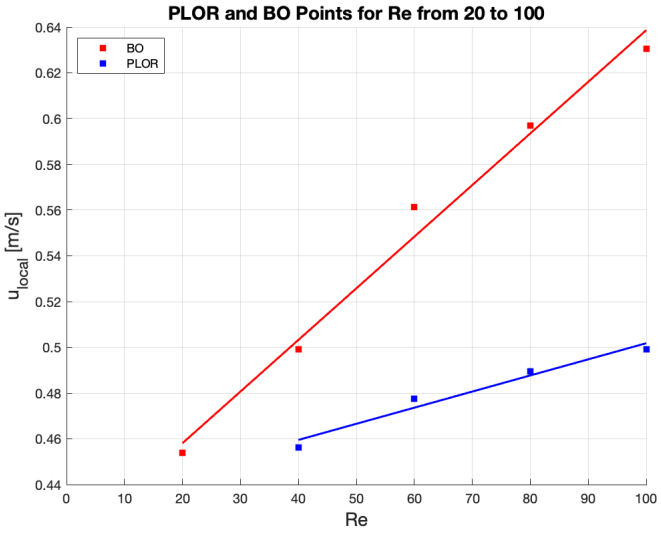

(b)

Figure 3.7: **Single Jet**: Scaling for the UCLA experimental results for periodic liftoff and reattachment (PLOR) and blow off (BO) as a function of jet Reynolds number: (a) local pressure perturbation amplitude at transition points (b) local velocity perturbation amplitude.

3.1.2 Pressure Antinode (PAN) Forcing

Our microjet acoustic experiments at UCLA were conducted near a PN, with a relatively large velocity perturbations and a bulk deflection from the PN, since the microjet flame did not have significant deflection or response at the pressure antinode (PAN). On the other hand, at AFRL, pressure-driven oscillations of the flame at a PAN are performed on various forcing frequencies. Unlike the turbulent flame at pressure node (PN), periodic liftoff and reattachment (PLOR) and complete flame blowout (full extinction or BO) transition points are achievable at the pressure antinode (or velocity node, where $u'_{local} = 0$).

As expected, there is not much similarity between the AFRL's pressure antinode (PAN) and our group's (UCLA EPRL) pressure node (PN) studies. However, looking at the oscillatory local pressure amplitude and the flame standoff distance from the AFRL PAN experiments in Figure 3.8, it is evident that an oval representing periodic liftoff and reattachment is formed. This suggests that further exploration of single flames in the vicinity of a PAN in the UCLA experiments could be fruitful.

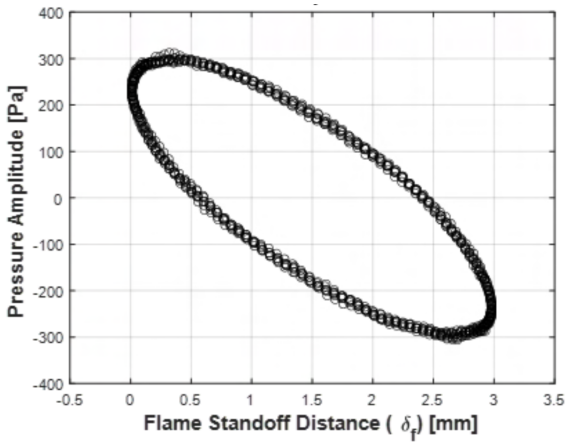

Figure 3.8: **Single Jet**: For PAN excitation in the AFRL experiments, local pressure measurements [Pa] vs. oscillations in flame standoff distance [mm] taken from [Plascencia Quiroz, 2021].

3.2 Coaxial Jet

The coaxial jet results discussed in this section have the following burner configurations. As shown in Figure 3.9, the AFRL coaxial burner has a low-velocity oxidizer co-flow which is not a part of our jet design at UCLA EPRL. Table 3.2 summarizes the dimensions of the two different coaxial burners used under turbulent and laminar flow conditions.

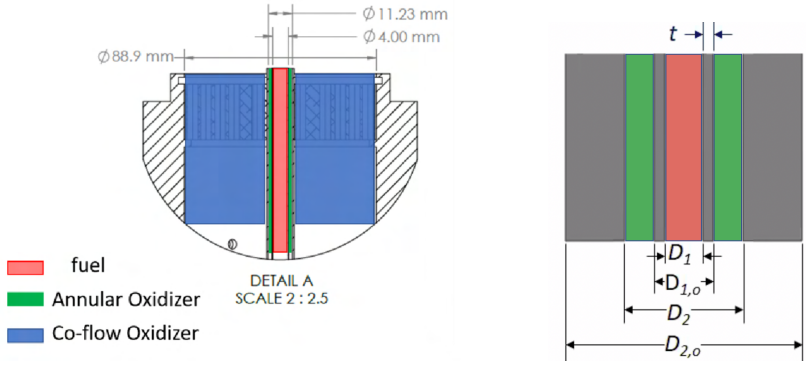

(a) (b)

Figure 3.9: **Coaxial Jet**: Burners' schematics. (a) AFRL's burner configuration with a center jet (inner diameter of 4.0 mm, post thickness of 0.36 mm, and annular oxidizer diameter of 11.23 mm) surrounded by an annular flow section (outer diameter of 88.9 mm) [Plascencia Quiroz, 2021]. (b) UCLA EPRL's burner schematic with an inner diameter of 1.02 mm and an annular outer diameter of 6.35 mm.

Table 3.2: AFRL and UCLA EPRL coaxial jet dimensions [Plascencia Quiroz, 2021].

Coaxial Burner	D_1[mm]	$D_{1,o}$[mm]	D_2[mm]	$D_{2,o}$[mm]	D_3[mm]
AFRL	4.00	4.72	11.23	11.95	88.9
UCLA EPRL	1.02	1.59	3.17	6.35	NA

Unlike single jet wherein the absence of external excitation, neither the AFRL nor UCLA detected natural flame instabilities; such natural instabilities have been observed in the

AFRL coaxial jet experiments close to a frequency of 1500 Hz (see Figure 3.10). However, there are no natural instabilities for the UCLA coaxial jet. It is suspected that such natural instabilities of the turbulent coaxial jet are associated with the shear layer modes [Plascencia Quiroz, 2021]. Thus, based on Figure 3.10, a coaxial jet under turbulent conditions exhibits a reactive shear layer behavior.

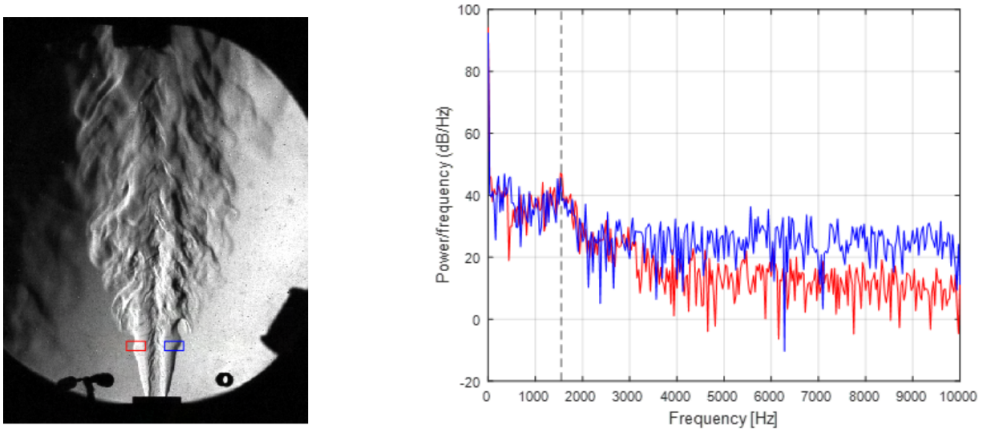

(a) (b)

Figure 3.10: **Coaxial Jet**: AFRL's Shear layer PSD analysis of coaxial jet with $R = 0.3$: (a) schlieren snapshot (b) power spectral densities (PSD) of integrated intensity signal a sequence of 2000 snapshots [Plascencia Quiroz, 2021].

3.2.1 Pressure Node (PN) Forcing

We now turn to a comparison of coaxial fuel/air jet injection in the acoustically resonant environments in the UCLA and AFRL experiments. Figure 3.11 shows comparisons, for example, of the first four POD modes for the AFRL and UCLA experiments, with an annular-to-jet velocity ratios of R =0.3, for all three cases. Here the nearly symmetrical coaxial turbulent flame is compared with a laminar coaxial flame under a relatively low and high forcing amplitude before and near the transitional stage between the PLOR and BO (transition to PLOR occurred at 145 Pa). The AFRL experiments also had bulk coflowing air outside of

the annular region; per experiments at AFRL for both the single jet and coaxial jet, having an external coflow helps in sustaining the flame.

Note that in Figure 3.11 the ratio of the local perturbation velocity to the jet velocity, u'/U_{jet}, for the AFRL (turbulent) and UCLA (laminar) cases are respectively 0.1, 0.5 and 0.6. As mentioned before, the laminar flame's high local to jet velocity ratio causes the flame to lie in the PLOR stage, with much more vigorous transverse perturbations to the flame. Figure 3.11(b) captures the flame at a stage right before PLOR transition (PLOR transition happens at 145 Pa). Looking at the modal energy content in Figure 3.11(a) and 3.11(c), it is evident that POM1 has greater energetic content for the AFRL experiment at a relatively low-velocity perturbation than the energy content in the UCLA experiment at a relatively higher velocity perturbation. However, comparing the pre-transition case in Figures 3.11(a) and 3.11(b), the energy contents are still different. Therefore, the AFRL case lies close to the PLOR transition point. For the UCLA experiments, PLOR phenomena are generally associated with a significant reduction in the energy content of the first proper orthogonal mode and distribution of the energy into other modes that represent the multiple frequencies associated with liftoff as well as flame-acoustic coupling [Sim et al., 2020]. Based on the energy distribution in Figure 3.11, it is evident that modes 1 and 2 dominate the oscillatory behavior of the flame in the AFRL experiments [Plascencia Quiroz, 2021], while at least the first four modes are required to characterize the UCLA laminar flame, since it has undergone a dynamical transition to PLOR.

Despite the differences in the cases shown in Fig. 3.11, dynamical characteristics between the experiments have some similarities. In Figures 3.12 and 3.13, the phase portrait coefficients are plotted against one another for the coaxial jet to study the flame dynamics. The POD modes of AFRL and UCLA EPRL in Figure 3.12 are not very comparable. However, looking at Figure 3.13, a similar dynamical coupling is observed. Both flames in Figure 3.13 exhibit a periodic harmonic pattern by their relatively oval shape in the a1 vs. a2 plot. Although the UCLA flames with PLOR are asymmetrical, the higher mode plots also have a

similar pattern between the two cases, indicating similar flame dynamics between the coaxial laminar and turbulent cases. This suggests that if a high enough amplitude of excitation in the vicinity of a PN were to be applied in the AFRL coaxial jet experiments, similar types of asymmetric dynamical characteristics, in addition potentially to PLOR, could be attained. This further indicates the value of exploring flame dynamics at low Reynolds numbers in enabling an understanding of the higher Re dynamics.

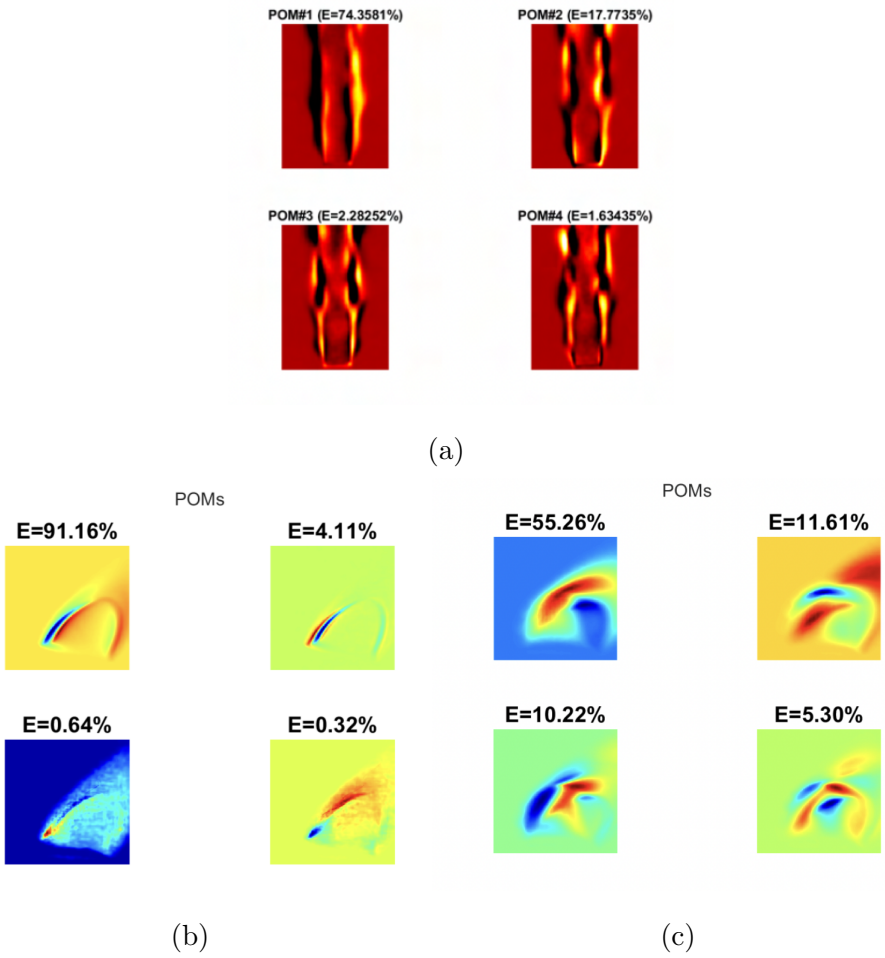

Figure 3.11: **Coaxial Jet**: POD plots for PN excitation. (a) AFRL's first four POD spatial modes with associated percentage of energetic content analysis results for 581 Hz excitation at an amplitude of 900 Pa ($u^{'} = 2.6$ m/s) at a PN with $U_{jet} = 24$ m/s ($u'/U_{jet} = 0.1$) and $R = 0.3$ [Plascencia Quiroz, 2021]. (b) EPRL's first four POD spatial modes with associated percentage of energetic content analysis results for 332 Hz excitation at an amplitude of 140 Pa ($u^{'} = 0.33$ m/s) near a PN with $U_{jet} = 0.66$ m/s or $Re_{jet} = 40$ ($u'/U_{jet} = 0.5$) and $R = 0.3$ [Vargas et al., 2021] (c) EPRL's first four POD spatial modes with associated percentage of energetic content analysis results for 332 Hz excitation at an amplitude of 160 Pa ($u^{'} = 0.38$ m/s) near a PN with $U_{jet} = 0.66$ m/s ($u'/U_{jet} = 0.6$) and $R = 0.3$ [Vargas et al., 2021].

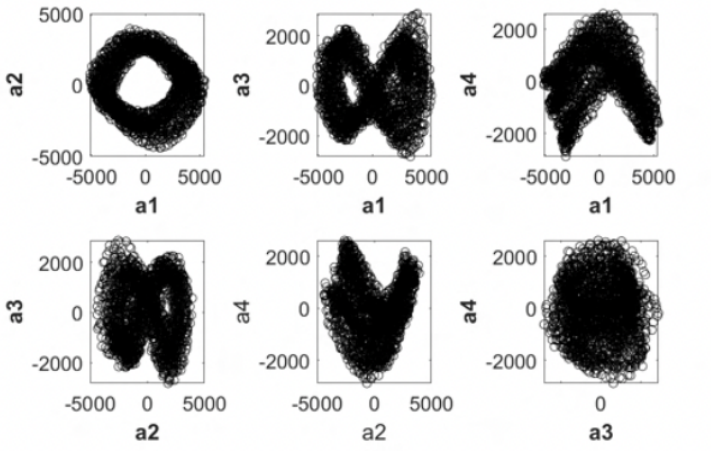

(a)

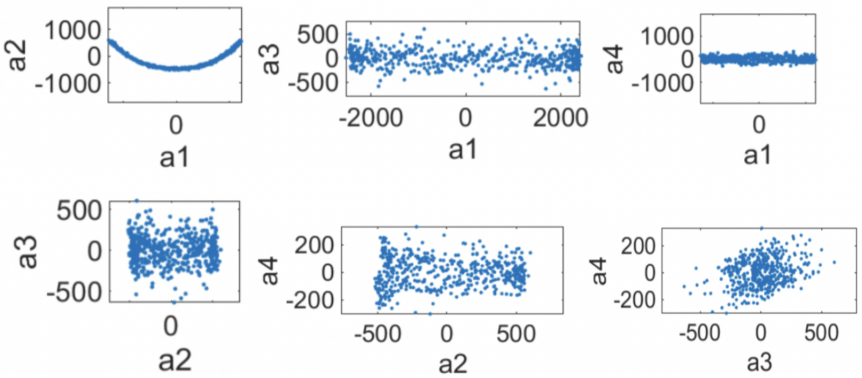

(b)

Figure 3.12: **Coaxial Jet**: POD plots. (a) AFRL's POD mode coefficients plotted against one another for the first four modes for 581 Hz excitation at an amplitude of 900 Pa ($u^{'} = 2.6$ m/s) at a PN with $U_{jet} = 24$ m/s ($u'/U_{jet} = 0.1$) and $R = 0.3$ [Plascencia Quiroz, 2021]. (b) EPRL's POD mode coefficients plotted against one another for the first four modes for 332 Hz excitation at an amplitude of 140 Pa ($u^{'} = 0.33$ m/s) near a PN with $U_{jet} = 0.66$ m/s or $Re_{jet} = 40$ ($u'/U_{jet} = 0.5$) and $R = 0.3$ [Vargas et al., 2021].

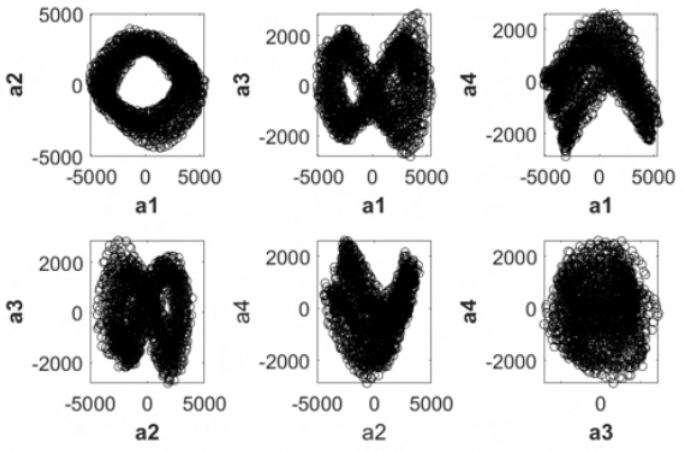

(a)

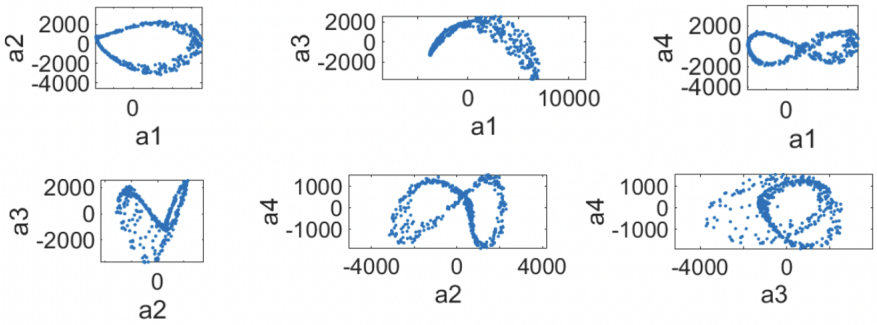

(b)

Figure 3.13: **Coaxial Jet**: POD plots. (a) AFRL's POD mode coefficients plotted against one another for the first four modes for 581 Hz excitation at an amplitude of 900 Pa ($u^{'} = 2.6$ m/s) at a PN with $U_{jet} = 24$ m/s ($u'/U_{jet} = 0.1$) and $R = 0.3$ [Plascencia Quiroz, 2021]. (b) EPRL's POD mode coefficients plotted against one another for the first four modes for 332 Hz excitation at an amplitude of 160 Pa ($u^{'} = 0.38$ m/s) near a PN with $U_{jet} = 0.66$ m/s or $Re_{jet} = 40$ ($u'/U_{jet} = 0.6$) m/s and $R = 0.3$ [Vargas et al., 2021].

3.2.2 Pressure Antinode (PAN) Forcing

For the pressure antinode (PAN), the coaxial jet's response to increasing forcing frequency contrasts that in a single jet in AFRL experiments (see Fig. 3.14). In the single jet, higher amplitude forcing is required at higher frequencies to obtain a flame response, while for the coaxial jet, lower amplitudes are required to get a flame response by increasing the forcing frequency. For instance for the coaxial jet, no transitional response is recorded at the forcing frequency of 360 Hz, while at 775 Hz, a periodic liftoff, and the permanent liftoff occurs at 450 Pa and 600 Pa [Plascencia Quiroz, 2021]. These differences may be explained by noting that the coaxial jet has a natural instability in these AFRL experiments at around 1500 Hz, and as this frequency is approached in external forcing, the jet naturally locks in to its natural mode, requiring a lower amplitude to achieve jet response [Shoji et al., 2020]. In contrast, the single jet does not have a detectable natural instability in the absence of forcing, and hence the diffusion flame requires higher amplitude excitation at higher frequencies, as long understood [Selerland and Karagozian, 1998]. Nevertheless, these differences suggest that additional studies are required for both single and coaxial jets, at AFRL and at UCLA.

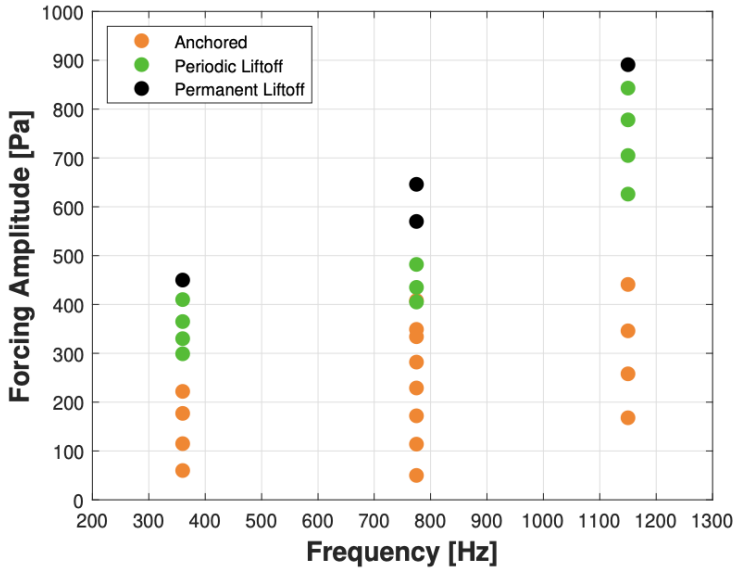

(a)

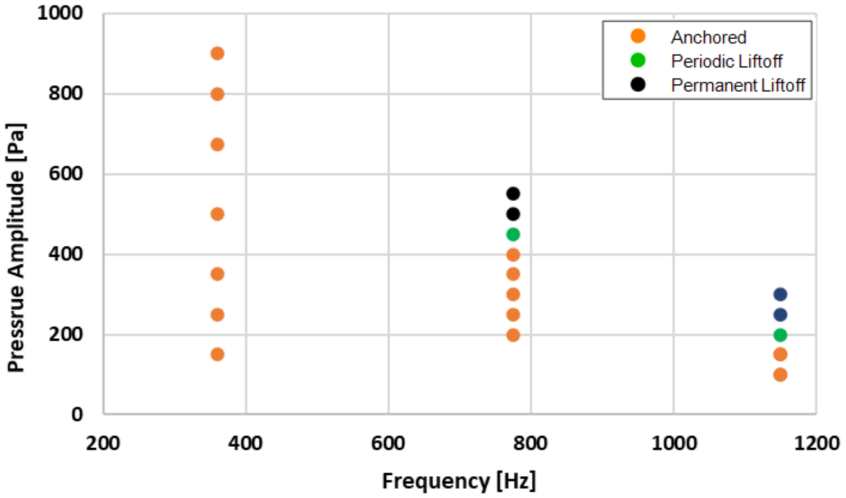

(b)

Figure 3.14: **Single vs. Coaxial Jet in AFRL experiments at the PAN:** pressure amplitude [Pa] vs. frequency [Hz] for (a) the single jet and (b) the coaxial jet at R=0.3 [Plascencia Quiroz, 2021].

CHAPTER 4

Conclusions and Recommendations for Future Studies

4.1 Summary

This thesis has described the similarities and differences between the acoustically coupled combustion studies performed at the AFRL and UCLA EPRL research facilities under laminar and turbulent conditions. In both research facilities, two alternative burner configurations of a single and coaxial jet are used to conduct the experiments. The burner configurations have a similar setup in both facilities, with the exception of the low-velocity oxidizer co-flow at the AFRL experiments to assist with anchoring of the turbulent flame.

To analyze the single jet flame dynamics under laminar and turbulent conditions, flame structures with relatively axisymmetric oscillatory shapes under acoustic forcing with Reynolds numbers of 65 and 5300 are compared. The single turbulent jet flow has a 581 Hz forcing frequency with the flame precisely at the pressure node (PN). While the laminar fuel jet in the UCLA experiments has a 332 Hz forcing frequency, and the flame is located near the not precisely at the PN. The PSD analysis of the laminar and turbulent single jet suggests the locking-in of the oscillating flame under the applied acoustic forcing. The POD modes of both cases have similar patterns and shapes, indicating a periodic traveling wave. In the laminar microjet case, the flame transition to PLOR and finally BO by increasing the forcing amplitude. However, AFRL configuration could not achieve high enough excitation levels to explore phenomena observed in transition to PLOR. Still, there are many similarities between the two laminar and turbulent flames under the pressure node (PN) acoustic forcing

conditions. No significant deflection or response was observed from the microjet at PAN, so no experiments were conducted. Thus, the PAN forcings are not comparable under laminar and turbulent conditions.

For the coaxial jet similar annular to inner jet velocity ratio of 0.3 is selected to compare the results under laminar and turbulent conditions. The turbulent coaxial jet exhibits natural instability near 1500 Hz, which indicates the shear-like behavior of the flame. Similar phase portraits are detected when comparing the turbulent coaxial jet and the laminar coaxial jet in the PLOR state. This is an indication of a turbulent flame being close to its transition point. Such similarities between the low and high Reynolds number jets enable one to better understand the high Reynolds number combustion by conducting small-scale experiments with microjets at low flow conditions. The ultimate goal is to gather enough data to generate a systematic Reduced Order Model (ROM) capable of predicting the flame instabilities at high Reynolds numbers without costly large-scale experiments.

4.2 Future Work

While this study has brought some insight into the dynamical similarities between the laminar and turbulent conditions of reacting jets under acoustic forcing, further investigation is required to analyze these patterns. Therefore, recommendations will focus on closing the gap between the laminar and turbulent regimes by characterizing a pattern between the two studies.

The first recommendation is to perform more extended experiments on the pressure node (PN) single turbulent flame at AFRL to explore possible transitional points. Determining trends such as those in the linear relations for the low Reynolds number experiments at UCLA could be helpful in future studies for estimating the required transitional amplitudes and possibly providing some additional insight in modeling the flames and controlling acoustically coupled combustion systems.

Another recommendation is to further explore the coaxial jet with various wall thicknesses for the laminar and the turbulent flames. Currently, the available data for the coaxial jet is not systematic enough to recognize a trend between the two regimes. In addition, a closer R ratio with similar scaled wall thickness could help understand each component's role in flame instability under acoustic forcing to establish a more systematic approach to the coaxial jet comparison. As another future direction, UCLA EPRL experiments could explore flame instability precisely at the pressure node (PN) which is the velocity antinode. Further, it would be helpful to collect pressure antinode (PAN) data for the microjet laminar flame to investigate the similarities and differences under the dominant pressure field. Lastly, exploring different fuel types could provide some insight into the chemical kinetics of the perturbed flame in addition to the dynamical aspect of the acoustic forcing.

Bibliography

J. W. Bennewitz, D. Valentini, M. A. Plascencia, A. Vargas, H. S. Sim, B. Lopez, O. I. Smith, and A. R. Karagozian. Periodic partial extinction in acoustically coupled fuel droplet combustion. *Combustion and flame*, 189:46–61, 2018.

G. Berkooz, P. Holmes, and J. L. Lumley. The proper orthogonal decomposition in the analysis of turbulent flows. *Annual Review of Fluid Mechanics*, 25(1):539–575, 1993.

S. Candel. Combustion dynamics and control: Progress and challenges. *Proceedings of the Combustion Institute*, 29(1):1–28, 2002.

S. M. Candel. Combustion instabilities coupled by pressure waves and their active control. *Symposium (International) on Combustion*, 24(1):1277–1296, 1992.

S. Chen, D. Zhao, H. K. H. Li, T. Y. Ng, and X. Jin. Numerical study of dynamic response of a jet diffusion flame to standing waves in a longitudinal tube. *Applied Thermal Engineering*, 112:1070–1082, 2017.

A. Choudhuri, J. Camacho, R. Wicker, and S. Gollahalli. Characteristics of micro-jet diffusion flames. In *38th AIAA/ASME/SAE/ASEE Joint Propulsion Conference & Exhibit*, 2002.

S. H. Chung and C. K. Law. Burke–schumann flame with streamwise and preferential diffusion. *Combustion Science and Technology*, 37(1-2):21–46, 1984.

F. E. Culick and V. Yang. Overview of combustion instabilities in liquid-propellant rocket engines. *Liquid Rocket Engine Combustion Instability*, 169:3–37, 1995.

S. Dattarajan, A. Lutomirski, R. Lobbia, O. Smith, and A. Karagozian. Acoustic excitation of droplet combustion in microgravity and normal gravity. *Combustion and Flame*, 144 (1-2):299–317, 2006.

L. S. De B. Alves, R. E. Kelly, and A. R. Karagozian. Transverse-jet shear-layer instabilities. part 2. linear analysis for large jet-to-crossflow velocity ratio. *Journal of Fluid Mechanics*, 602:383–401, 2008. doi: 10.1017/S002211200800102X.

S. Ducruix, T. Schuller, D. Durox, and S. Candel. Combustion dynamics and instabilities: Elementary coupling and driving mechanisms. *Journal of Propulsion and Power*, 19(5): 722–734, 2003.

P. Holmes, J. L. Lumley, G. Berkooz, and C. W. Rowley. *Turbulence, Coherent Structures, Dynamical Systems and Symmetry*. Cambridge University Press, 2012.

A. R. Karagozian. Acoustically Coupled Combustion of Liquid Fuel Droplets. *Applied Mechanics Reviews*, 68(4), 07 2016. ISSN 0003-6900. doi: 10.1115/1.4033792. URL `https://doi.org/10.1115/1.4033792`. 040801.

S. C. Li, A. S. Gordon, and F. A. Williams. A simplified method for the computation of burke-schumann flames in infinite atmospheres. *Combustion Science and Technology*, 104 (1-3):75–91, 1995. doi: 10.1080/00102209508907711. URL `https://doi.org/10.1080/00102209508907711`.

T. Lieuwen, H. Torres, C. Johnson, and B. T. Zinn. A Mechanism of Combustion Instability in Lean Premixed Gas Turbine Combustors . *Journal of Engineering for Gas Turbines and Power*, 123(1):182–189, 04 2000. ISSN 0742-4795. doi: 10.1115/1.1339002. URL `https://doi.org/10.1115/1.1339002`.

K. McManus, T. Poinsot, and S. M. Candel. A review of active control of combustion instabilities. *Progress in Energy and Combustion Science*, 19(1):1–29, 1993.

S. Megerian, J. Davitian, L. S. De B. Alves, and A. R. Karagozian. Transverse-jet shear-layer instabilities. part 1. experimental studies. *Journal of Fluid Mechanics*, 593:93–129, 2007. doi: 10.1017/S0022112007008385.

K. E. Meyer, J. M. Pedersen, and O. Özcan. A turbulent jet in crossflow analysed with proper orthogonal decomposition. *Journal of Fluid Mechanics*, 583:199–227, 2007.

D. Norton and D. Vlachos. Combustion characteristics and flame stability at the microscale: a cfd study of premixed methane/air mixtures. *Chemical Engineering Science*, 58(21): 4871–4882, 2003. ISSN 0009-2509. doi: https://doi.org/10.1016/j.ces.2002.12.005. URL https://www.sciencedirect.com/science/article/pii/S0009250903003877. International Symposium on Mathematics in Chemical Kinetics and Engineering.

J. C. Oefelein and V. Yang. Comprehensive Review of Liquid-propellant Combustion Instabilities in F1 Engines. *Journal of Propulsion and Power*, 9(5):657–677, 1993.

M. A. Plascencia Quiroz. Combustion dynamics of liquid droplets and turbulent jets relevant to rocket engines. *Ph.D. thesis*, 2021.

Preetham, H. Santosh, and T. Lieuwen. Dynamics of laminar premixed flames forced by harmonic velocity disturbances. *Journal of Propulsion and Power - J PROPUL POWER*, 24:1390–1402, 11 2008. doi: 10.2514/1.35432.

L. Rayleigh. The explanation of certain acoustical phenomena. *Nature*, 18:319–321, July 1878. URL http://www.nature.com/nature/journal/v18/n455/pdf/018319a0.pdf.

K. Saito, F. A. Williams, and A. S. Gordon. Structure of Laminar Coflow Methane–Air Diffusion Flames. *Journal of Heat Transfer*, 108(3):640–648, 08 1986. ISSN 0022-1481. doi: 10.1115/1.3246984. URL https://doi.org/10.1115/1.3246984.

P. J. Schmid. Dynamic mode decomposition of numerical and experimental data. *Journal of Fluid Mechanics*, 656:5–28, 2010.

T. Selerland and A. R. Karagozian. Ignition, burning and extinction of a strained fuel strip with complex kinetics. *Combustion Science and Technology*, 131(1-6):251–276, 1998. doi: 10.1080/00102209808935763. URL https://doi.org/10.1080/00102209808935763.

C. I. Sevilla Esparza. *Oscillatory Flame Response in Acoustically Coupled Fuel Droplet Combustion*. PhD thesis, UCLA, 2013.

C. I. Sevilla-Esparza, J. L. Wegener, S. Teshome, J. I. Rodriguez, O. I. Smith, and A. R. Karagozian. Droplet combustion in the presence of acoustic excitation. *Combustion and Flame*, 161(6):1604–1619, 2014.

T. Shoji, E. W. Harris, A. Besnard, S. G. Schein, and A. R. Karagozian. Transverse jet lock-in and quasiperiodicity. *Phys. Rev. Fluids*, 5:013901, Jan 2020. doi: 10.1103/PhysRevFluids.5.013901. URL `https://link.aps.org/doi/10.1103/PhysRevFluids.5.013901`.

H. S. Sim, M. A. Plascencia, A. Vargas, and A. R. Karagozian. Acoustically forced droplet combustion of liquid fuel with reactive aluminum nanoparticulates. *Combustion Science and Technology*, 192(5):761–785, 2019. doi: 10.1080/00102202.2019.1593971. URL `https://doi.org/10.1080/00102202.2019.1593971`.

H. S. Sim, A. Vargas, D. D. Ahn, and A. R. Karagozian. Laminar microjet diffusion flame response to transverse acoustic excitation. *Combustion Science and Technology*, 192(7):1292–1319, 2020.

A. Vargas. Acoustically coupled, non-premixed combustion processes. *Ph.D. prospectus*, 2019.

A. Vargas, J. Guerrero, S. Kiani, and A. Karagozian. Laminar flame dynamics of multi-port fuel jets under acoustic forcing. In *APS Division of Fluid Dynamics Meeting Abstracts*, pages Z12–002, 2020.

A. Vargas, S. Kiani, and A. R. Karagozian. Dynamics of coaxial methane-air jets under acoustic forcing. *APS*, 602:383–401, 2021. doi: 10.1017/S002211200800102X.

A. D. Weiss, W. Coenen, A. L. Sánchez, and F. A. Williams. The acoustic response of

burke–schumann counterflow flames. *Combustion and Flame*, 192:25–34, 2018. ISSN 0010-2180.

Z. Wu, D. Laurence, S. Utyuzhnikov, and I. Afgan. Proper orthogonal decomposition and dynamic mode decomposition of jet in channel crossflow. *Nuclear Engineering and Design*, 344:54–68, 2019.